MASTER THESIS:

ANALYSIS OF THE YB ISOTOPE SHIFT IN CONNECTION TO DARK MATTER

MASTER IN NUCLEAR PHYSICS

Author:

Martí Circuns i Duxans

Advisors:

Javier Menéndez & Arnau Rios Huguet

UNIVERSITAT DE BARCELONA

Dept. Física Quàntica i Astrofísica

Facultat de Física

Universitat de Barcelona

November 2021

This page has been intentionally left blank.

En memòria del tiet Rafa i la iaia Antònia.
El vostre record serà sempre un tresor.

This page has been intentionally left blank.

Acknowledgements

I would like to express my sincere gratitude to Prof. Javier Menéndez and Prof. Arnau Rios for their valuable comments, interesting discussions, kind guidance and empathy along this Master's Thesis. I would also want to thank my family, my colleagues and Arleen for their unconditional love and support. This work is as much yours as mine.

This page has been intentionally left blank.

Contents

This page has been intentionally left blank.

1. Introduction

1.1. Motivation

Developed in the early 1970s, the Standard Model (SM) of particle physics is nowadays one of the most successful theories in physics, being able to unify three out of the four fundamental forces in nature. Despite the fact that the SM explains quite successfully almost all experimental results, in addition to the prediction of a wide variety of physical phenomena, some indirect evidences may point towards physics beyond the SM, also known as New Physics. This evidence includes the preponderance of dark matter (DM) in the universe. DM has been indirectly observed through many astronomical and cosmological observations such as the rotation curves of galaxies [1], gravitational lensing [2], the motion of colliding galaxy clusters [3] and the power spectrum of the cosmic microwave background [4]. DM candidates can be characterised principally by their interactions, mass and spin and even though they do not interact with light, we can not exclude that they can interact with ordinary matter

This Master's thesis has been mainly motivated by the work done in Ref.[5], where it has been measured the isotope shifts for five Yb^+ isotopes with zero nuclear spin on two narrow optical transitions with an unprecedented accuracy . The corresponding King's plot -which results, to a very good approximation, in a linear relation between the differences of both frequencies- showed a 3×10^{-7} deviation from linearity at 3σ uncertainty level. On the one hand, the origin of these non-linearities may indicate physics beyond the SM in the form of a new bosonic force carrier [6] that, in principle, may be compatible with the existence of a dark-matter candidate in the intermediate mass range from $\sim 100eV/c^2$ to $\sim 100MeV/c^2$ [7], see fig. 1.1. On the other hand, these nonlinearities may arise from higher-order nuclear effects within the SM. It was claimed that the quadratic field shift (QFS) was likely to explain the observed nonlinearities at the observed scale. However, recent work done in Ref.[8] predicts nuclear deformation as a source of the non-linearity of King's plot for Yb^+ ion. In order to do so, they took state-of-the-art nuclear models which all predicted a strong quadrupole deformation for every even-even neighbouring Yb isotope.

Figure 1.1.: Representation of the new intra-atomic force between an atomic electron (e^-) and a nuclear neutron (n). The resulting interaction is mediated by the exchange of an hypothetical new boson, ϕ, called *Dark-Boson*, which couples to quarks and leptons. The virtual exchange of ϕ would result in a Yukawa-like potential.

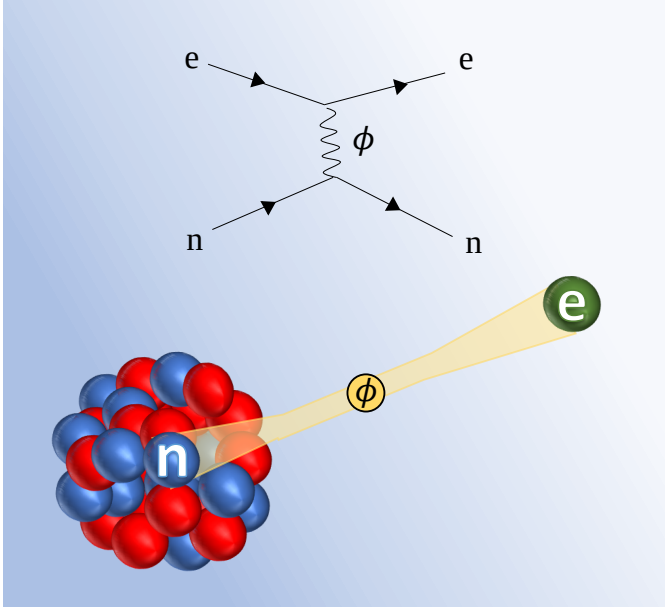

The main objective of this thesis is to improve the calculations done by [5] and [8] with the mean-field nuclear code SKYAX [9] using energy-density functionals to calculate the nuclear structure of Yb isotopes relevant for isotope shift measurements.

1.2. Isotope Shift theory in atomic spectra

Let's now get quantitative and try to achieve an insight on isotope shift theory. Consider the two narrow optical quadrupole transitions, $\alpha \equiv {}^2S_{1/2} \rightarrow {}^2D_{5/2}$ and $\beta \equiv {}^2S_{1/2} \rightarrow {}^2D_{3/2}$, for a given isotope of Yb^+ ion represented in fig. 1.2. Their transition frequency, ν_α and ν_β are represented by Greek subscripts, which, along this work, will denote isotope-independent, transition-dependent parameters.

Even though an atomic spectral line is characteristic of the element producing the spectrum, the energy of a spectral lines does indeed depend slightly on the isotope. Because of that, there is a tiny but measurable difference when one compares the transition frequency of one isotope with respect to another. As a consequence, the isotope shift is defined as the difference between a single electronic level of different isotopes of the same element. Consider two Yb^+ ions, one corresponding to isotope j and the other to

Figure 1.2.: The two narrow optical quadrupole transitions, α and β, of Yb^+ ion.

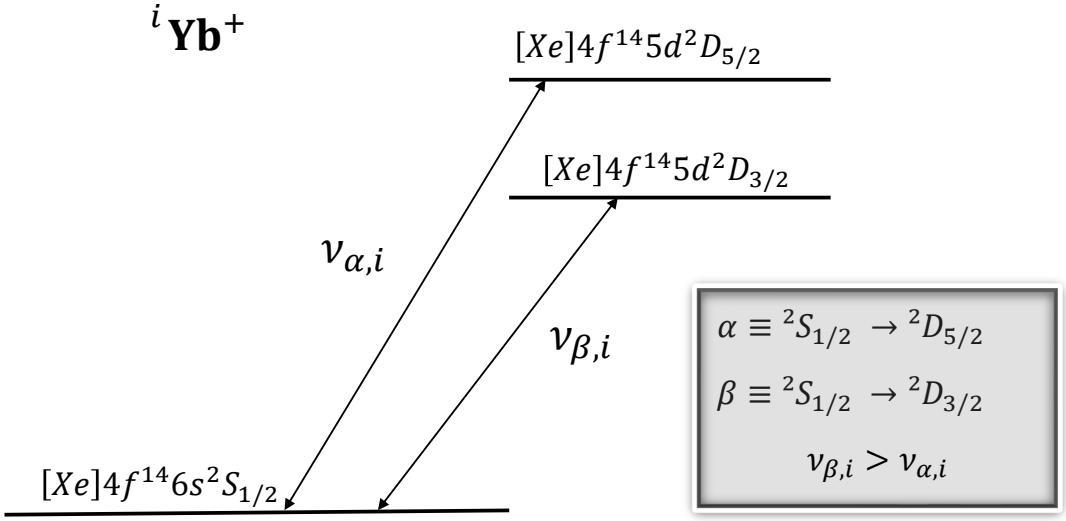

isotope i. Now let us assume that j and i indicate the number of nucleons of each isotope. Then both transition frequencies are be denoted as $\nu_{\alpha,j}$ and $\nu_{\alpha,i}$. The frequency shift is defined as

$$\nu_{\alpha,ji} \equiv \nu_{\alpha,j} - \nu_{\alpha,i}. \tag{1.1}$$

Bearing in mind the definition of isotope shifts given above, one could ask about the physical origin of this shift when one compares the same transition between two given Yb^+ isotopes. Firstly, we are dealing with isotopes of the same element. Thus, one could intuitively think that this phenomena is due to the mass difference between isotopes, which is indeed a very good point [1]. Each atomic level is described by an eigenfunction with eigenvalues of angular momentum and energy. As the angular momentum has a definite value, if one varies the mass of the atomic nucleus by replacing one isotope for another, the energy of the level is forced to change in order to remain with the same angular momentum. This effect is called mass shift (MS) and is due to a variation in nuclear mass from one isotope to another. This term is often understood as a contribution of a change in nuclear recoil, denominated as normal mass shift, and a change in electron-electron correlations, known as specific mass shift [6, 10]. Nonetheless, both effects are

[1] This mass dependence was firstly suggested with the advent of Bohr's theory of the structure of the atom in 1913 [10]

proportional to the inverse-mass difference, μ_{ji}:

$$\mu_{ji} = \frac{1}{m_j} - \frac{1}{m_i}, \tag{1.2}$$

where m_j and m_i are the masses of the nuclei of the two isotopes [6, 11].

The MS is not the only cause of isotope shift in atomic spectra. Even though isotopes, by definition, share the same number of protons[2], they do not have the same spatial distribution over the nucleus as they do not share the same number of neutrons. Therefore, the nuclear charge distribution is affected by the difference in neutron number. As a consequence, the variation of the charge distribution of the nucleus from one isotope to another produces a noticeable effect called field shift (FS). The FS originates from the change in the nuclear charge radius, which leads to different electronic potentials near the origin of the nucleus. FS theory was settled by Seltzer [12] and afterwards in [13] following developments which took nearly one century.

Broadly speaking, both contributions - MS and FS- explain most of the experimental isotope shift phenomena in atomic spectra. The isotope shift between j and i isotopes of a given atomic transition, e.g. α, is usually decomposed into the sum of both MS and FS terms [3]:

$$\nu_{\alpha,ji} = \nu^{MS}_{\alpha,ji} + \nu^{FS}_{\alpha,ji}. \tag{1.3}$$

The MS takes into account the variation from one isotope to another in nuclear mass and it is proportional to the inverse-mass difference, see eq. (1.2). On the other hand, the field shift is due to the variation of the charge distribution of the nucleus and it is approximately proportional to the difference in the squared charge radius, $\delta\langle r^2\rangle_{ji}$:

$$\delta\langle r^2\rangle_{ji} = \langle r^2\rangle_j - \langle r^2\rangle_i, \tag{1.4}$$

where $\langle r^2\rangle$ is the squared charge radius which depends on the isotope. The root-mean-squared (rms) charge radius, $\langle r^2\rangle^{1/2}$ provides information about the size of an atomic nucleus, particularly the proton distribution. In addition to that, the point-proton radius of a given isotope, $R_{p,i}$, can be related to the rms charge radius as follows [15]:

$$\langle r^2\rangle_i = R^2_{p,i} + \langle r^2_p\rangle + \langle r^2_p\rangle_{so,i} + \frac{N}{Z}\Big(\langle r^2_n\rangle + \langle r^2_n\rangle_{so,i}\Big), \tag{1.5}$$

[2] Etymologically, the word *isotope* is derived from the Greek: *isos* (equal) and *topos* (place), and was historically conceived by Soddy in 1913 with its actual meaning. Thus, one refers to isotopes as a set of atomic elements which have the same atomic number, Z, thus share the same number of protons, but differ in the number of neutrons, N.

[3] We would like to highlight that experimental anomalies in the optical isotope shifts of Samarium challenged eq. (1.3), see [14]

where $\langle r_n^2 \rangle_{so}$ is the neutron spin-orbit contribution, $\langle r_p^2 \rangle_{so}$ is the proton spin-orbit contribution, $\langle r_p^2 \rangle$ is the electromagnetic mean-square radius of the proton, $\langle r_n^2 \rangle$ is the electromagnetic mean-square radius of the neutron and R_p is the point-proton radius. Purely isotope-dependent quantities or nuclear quantities will be denoted henceforth by latin subscripts which, in fact, denote the associated to the number of nucleons, A, of each isotope. The point-proton radius given by

$$R_p = \sqrt{\frac{\int dV(\mathbf{r} - \mathbf{R_p})^2 \rho_p(\mathbf{r})}{\int dV \rho_p(\mathbf{r})}}, \tag{1.6}$$

where dV is the volume element, $\rho_p(\mathbf{r})$ is the local proton density and

$$\mathbf{R}_p = \frac{\int dV \mathbf{r} \rho_p(\mathbf{r})}{\int dV \rho_r(\mathbf{r})} \tag{1.7}$$

is the center of mass moment. The local proton density can be computed from density functional theory [9, 16] and it is not necessarily the same as the charge density ρ_c which gives rise to eq. (1.5). In fact, this quantity will be provided by the nuclear mean-field code used in this work, see chapter 2.

The MS, for a given electronic transition, can be decomposed as a product of two terms and is given by.

$$\nu_{\alpha,ji}^{MS} = K_\alpha \mu_{ji}, \tag{1.8}$$

where K_α is an atomic parameter. K_α is a purely transition-dependent, isotope-independent parameter and μ_{ji} is the inverse-mass difference, an isotope-dependent parameter. The field shift can be also teared apart into the product of two terms, see Appendix A:

$$\nu_{\alpha,ji}^{(FS)} = \sum_{n=2}^{\infty} H_\alpha^{(n)} \delta\langle r^n \rangle_{ji} = H_\alpha^{(2)} \delta\langle r^2 \rangle + \mathcal{O}(\delta\langle r^4 \rangle_{ji}) \simeq F_\alpha \delta\langle r^2 \rangle_{ji}, \tag{1.9}$$

where the first non-zero term is the leading contribution to the field isotope shift and $F_\alpha \equiv H_\alpha^{(2)}$. Adding both mass shift, eq. (1.8), and field shift, eq. (1.9), we can eventually write down the isotope shift for a given atomic α transition.

$$\nu_{\alpha,ji} = K_\alpha \mu_{ji} + F_\alpha \delta\langle r^2 \rangle, \tag{1.10}$$

where F_α is the FS atomic parameter.

We would like to stress that eq. (1.10) is an approximation due to the truncation used in eq. (1.9). However, this is a good starting point as eq. (1.10) takes into account both major contributions in isotope shift measurements.

1.3. King's Linearity

In this section we derive a linear relation between both frequency shifts - $\nu_{\alpha,ji}$ and $\nu_{\beta,ji}$- the so-called King's linearity [10]. Consider both α and β narrow optical quadrupole transitions of Yb^+ shown in fig. 1.2. Their isotope frequency shifts are given by eq. (1.10):

$$\nu_{\alpha,ji} = K_\alpha \mu_{ji} + F_\alpha \delta\langle r^2\rangle_{ji}, \tag{1.11}$$

$$\nu_{\beta,ji} = K_\beta \mu_{ji} + F_\beta \delta\langle r^2\rangle_{ji}. \tag{1.12}$$

In order to obtain King's relation we first normalise eq. (1.11) and eq. (1.12) by the inverse-mass difference, μ_{ji}:

$$m\nu_{\omega,ji} \equiv \frac{\nu_{\omega,ji}}{\mu_{ji}}, \qquad \omega = \alpha, \beta, \tag{1.13}$$

where $m\nu_{\omega,ji}$ is the modified frequency shift induced by the isotope pair (j,i) and atomic transition ω. This leads to:

$$m\nu_{\alpha,ji} = K_\alpha + F_\alpha m\delta\langle r^2\rangle_{ji}, \tag{1.14}$$

$$m\nu_{\beta,ji} = K_\beta + F_\beta m\delta\langle r^2\rangle_{ji}, \tag{1.15}$$

where $m\delta\langle r^2\rangle_{ji}/\mu_{ji}$ is the modified frequency shift. Combining eq. (1.14) and eq. (1.15) yields

$$m\nu_{\beta,ji} = F_{\beta\alpha} m\nu_{\alpha,ji} + K_{\beta\alpha}, \tag{1.16}$$

where $F_{\beta\alpha} \equiv F_\beta/F_\alpha$ and $K_{\beta\alpha} \equiv K_\beta - F_{\beta\alpha}K_\alpha$. Equation (1.16) is the so-called King's relation and its graphical representation is known as King's plot [10]. Notice that, if experimental is consistent with King's linearity, eq. (1.16) provides a powerful tool in order to extract its slope and offset by plotting the measured frequency shifts one against the other for several isotope pairs [10] without any atomic physics calculations. In addition, this enables the extraction of relevant nuclear quantities such as $\delta\langle r^2\rangle$, the charge radius $\langle r^2\rangle^{1/2}$ and the inverse-mass difference, for example.

1.4. Beyond King's relation

Despite the relevance that King's plot has in revealing some important features of the atomic nuclei, in this subsection we are going to describe some higher order terms within the SM that may account for the observed non-linearities in [5] for a set of neighbouring even-even isotope pairs of Yb^+. In the previous section it has been shown that a linear relationship can be established between isotope shifts of two different transitions. As a consequence, the breaking of King's linearity is a direct evidence that small non-linearities

are present in Yb^+ ion, and therefore we must include additional contributions that can explain the experimental evidence. For instance, we could add a third term, namely $\delta\nu_{NL}$, in eq. (1.16) which accounts for those non-linear (NL) terms that are responsible for the current experimental findings of [5]:

$$m\nu_{\beta,ji} = F_{\beta\alpha} m\nu_{\alpha,ji} + K_{\beta\alpha} + m\delta\nu_{NL}, \tag{1.17}$$

where $m\delta\nu_{NL} \equiv \delta\nu_{NL}/\mu_{ji}$ is the modified NL frequency shift.

In fact, King's relation only considers the leading-order term of Seltzer's moment expansion in the field isotope shift, see eq. (1.9), and the inclusion of higher-order terms, see Appendix A, may contribute to the non-linearity. The origin of these small non-linearities in the Yb^+ remains still unclear and in this work we will only consider those NL terms that are within the SM, therefore disregarding the hypothetical dark boson contribution. In order to characterise the experimental evidence of small non-linearities in King's Plot, we rewrite both modified isotope shifts, accordingly to [8], as

$$m\nu_{\alpha,ji} = K_\alpha + F_\alpha m\delta\langle r^2\rangle_{ji} + G_\alpha^{(2)} m\left[\delta\langle r^2\rangle_{ji}\right]^2 + G_\alpha^{(4)} m\delta\langle r^4\rangle_{ji}, \tag{1.18}$$

$$m\nu_{\beta,ji} = K_\beta + F_\beta m\delta\langle r^2\rangle_{ji} + G_\beta^{(2)} m\left[\delta\langle r^2\rangle_{ji}\right]^2 + G_\beta^{(4)} m\delta\langle r^4\rangle_{ji}, \tag{1.19}$$

where $G_\alpha^{(2)}$, $G_\beta^{(2)}$, $G_\alpha^{(4)}$, $G_\beta^{(4)}$ are atomic parameters and $m\delta\langle r^4\rangle_{ji} \equiv \delta\langle r^4\rangle_{ji}/\mu_{ji}$, where $\delta\langle r^4\rangle_{ji}$ is the next leading order in Seltzer moment expansion of the FS, see Appendix A, and it is defined as follows

$$\delta\langle r^4\rangle_{ji} = \langle r^4\rangle_{p,j} - \langle r^4\rangle_{p,i}, \tag{1.20}$$

where $\langle r^2\rangle$ is the fourth order charge radius and, as we will see in chapter 3, this quantity can be computed by means of the fourth moment point-proton radius R_{p4}^4 in addition to some corrective terms. The fourth moment point-proton radius is not implemented in SkyAx. However, we implemented the following prescription of R_{p4}:

$$\langle r^4\rangle_p{}^{1/4} = \sqrt[4]{\frac{\int dV(\mathbf{r}-\mathbf{R_p})^4\rho_p(\mathbf{r})}{\int dV\rho_p(\mathbf{r})}}, \tag{1.21}$$

into the nuclear code.

On the one hand, the third term in eqs. (1.18) and (1.19) is known as the quadratic field shift (QFS) due to the second-order effect in the change of the nuclear Coulomb potential. On the other hand the fourth term is the fourth order radial moment shift (FOMS). Its origin is mainly due to relativistic effects in the electron wave function [8]. Both QFS and FOMS terms represent different physical phenomena [8]. Repeating the same procedure as in eq. (1.15) leads to

$$m\nu_{\beta,ji} = K_{\beta\alpha} + F_{\beta\alpha} m\nu_{\alpha,ji} + G_{\beta\alpha}^{(2)} m\left[\delta\langle r^2\rangle_{ji}\right]^2 + G_{\beta\alpha}^{(4)} m\delta\langle r^4\rangle_{ji}, \tag{1.22}$$

where $G^{(k)}_{\beta\alpha} \equiv \left(G^{(k)}_{\beta} - F_{\beta\alpha}G^{(k)}_{\alpha}\right)$ with $k \in \{2,4\}$. We would like to highlight that the first and the second term in eq. (1.22) reproduce the linear relation between both modified frequency shifts, $m\nu_{\beta,ji}$ and $m\nu_{\alpha,ji}$, In contrast, the third and fourth terms represent NL contributions to King's plot which might potentially account for the experimentally measured deviation from King's linear relation. Thus, from a theoretical point of view, it is of high priority to understand and quantify the impact of both NL contributions. The authors of Ref.[5] assume a simple correlation between $\langle r^4\rangle$ and $\langle r^2\rangle$:

$$\langle r^4\rangle_i = b\langle r^2\rangle_i^2, \tag{1.23}$$

where $b \approx 1$ is identical over different isotopes.

Alternatively, in Ref.[8] it is argued that nuclear deformation may lead to a nonlinearity of the King's plot. It is well known from both experimental [17] and its theoretical interpretation [18, 19] of nuclear rotational spectra that all neighbouring even-even isotopes of Yb studied in [5] have deformed nuclear ground states with a dimensionless quadrupole deformation, β_2, being approximately $\beta_2 \approx 0.3$. Therefore, in [8], the nuclear deformation is taken into account for the calculation of the field isotope shift in even-even Yb isotopes. Strong correlations between experimental and theoretical data are found, meaning that nuclear deformation may have a noticeable impact on the deviation from King's linearity. This has an impact on the magnitude of the deviation produced by each NL term. Indeed, it is found that the deviation coming from the QFS term drops about an order of magnitude being the FOMS the main source of non-linearity. This conclusion is opposed to [5], where the main source of non-linearity was due to the QFS term.

However, neither [5] nor [8] take into account theoretical uncertainties in their estimation of NL terms in eq. (1.22). In this work we will study the QFS and FOMS contributions including theoretical uncertainties using several state-of-the-art non-relativistic energy density functionals. In the forthcoming section we shall introduce a two spatial dimension, axially-symmetric, Hartree-Fock + BCS code called SkyAx, [9]. We use this nuclear code to predict a variety of properties of nuclear ground states for the set of ^{A}Yb isotopes of interest, with $A = \{168, 170, 172, 174, 176\}$. The obtained nuclear properties will provide both the nuclear and atomic input to study eq. (1.22) with different Skyrme parametrisations, pairing interactions and pairings schemes. The transition-dependent parameters, $K_{\beta\alpha}, F_{\beta\alpha}, G^{(2)}_{\beta\alpha}$ and $G^{(4)}_{\beta\alpha}$, shall be extracted from [5] and [8]. Eventually, we shall associate an error to each computed nuclear property due to code's resolution.

2. Nuclear structure calculations

The aim of this chapter is to introduce the 2D axially-symmetric nuclear code, SKYAX[9], used throughout this work. SKYAX determines axially symmetric, time-reversal invariant, stationary solutions to the self-consistent mean-field model based on Skyrme energy functional augmented by a density-dependent pairing functional and optionally by a constraint on low-order multipole moments [9]. SKYAX enables us to obtain fundamental nuclear properties such as the point-proton radius, for example. As a matter of fact, nuclear information will be of utter importance to compute important features about isotope shifts of even-even neighbouring Yb isotopes. SKYAX has a wide variety of Skyrme forces that can be selected in the input file in order to obtain the nuclear properties but with different Skyrme parametrisations, pairing interactions and pairing shcemes.

This chapter is structured as follows. In section 2.1 we introduce the Skyrme-Hartree-Fock (SHF) theory. Eventually, in section 2.2 we characterise how precise is SKYAX obtaining the nuclear properties of interest, hence quantifying the error due to the code's precision.

2.1. Skyrme-Hartree-Fock theory

There are several situations of highly correlated many-body systems where a full treatment is beyond current analytical, or even numerical capabilities. For example, the nucleus of an atom can be conceived as a finite, quantum-mechanical many-body system where the nucleons -protons and neutrons- are governed by the nuclear interaction. Despite the fact that nuclear interaction combines both a strong attraction and an enormous short-range repulsion, a simpler phenomenological treatment such as the independent nuclear shell model allows one to arrange all structural properties and basic low-energy excitations in the range up to giant resonances [16]. The assumption that nucleons move independently in an average potential produced by all of the nucleus is thus justified by the success of the phenomenological shell model. However, these models are limited by their empirical nature, as well as the neglected residual interactions between nucleons.

Noteworthy advantages emerge from the HF method as a better microscopic understanding is achieved due to the fact that in self-consistent mean-field models, the mean-

field Hamiltonian is not explicitly prescribed but generated from the many-body system itself [9].

The foundation for the HF setup starts with assuming a Hamiltonian which contains a one-body part which takes into account the kinetic energy of each nucleon and a one-body potential, denoted by $\hat{T}$, and a two-body interaction, denoted by $\hat{V}$. In coordinate space this looks like

$$\hat{H} = \hat{T} + \hat{V} = \sum_{k=1}^{A} \left[\frac{-\hbar^2}{2m} \bigtriangledown_k^2 + U_{ext}(x_k) \right] + \frac{1}{2} \sum_{k,l=1}^{A} v(x_k, x_l, ...),$$

where the indices of summation stand for the nucleons, x stands for the spatial coordinates and spin: $x_k = \{\boldsymbol{r_k}, \hat{\boldsymbol{\sigma}}_k\}$ and A stands for the total number of nucleons of particles k and l. The dots inside the two-body interaction indicate that the potential might depend on additional properties like their momenta and possibly isospins. The one-body part of the Hamiltonian accounts for the kinetic energy and one-body potential.

In terms of the second quantization and Fermi anihilation $\hat{a}$, and creation $\hat{a}^\dagger$ operators, the Hamiltonian can be written as

$$\hat{H} = \sum_{\alpha\beta} t_{\alpha\beta} \hat{a}_\alpha^\dagger \hat{a}_\beta + \frac{1}{2} \sum_{\alpha\beta\gamma\delta} v_{\alpha\beta\gamma\delta} \hat{a}_\alpha^\dagger \hat{a}_\beta^\dagger \hat{a}_\delta \hat{a}_\gamma, \tag{2.1}$$

where the indices α, β, γ and δ label the single-particle states in some complete orthonormal basis, $t_{\alpha\beta}$ refers to the kinetic energy and the $v_{\alpha\beta\gamma\delta}$ are the matrix elements of the two-body interaction. The eigenstates of this Hamiltonian are determined by the stationary Schrödinger's equation

$$\hat{H}|\Psi\rangle_{exact} = E_{exact}|\Psi\rangle_{exact}. \tag{2.2}$$

In virtue of the variational principle, one can show that the Schrödinger equation, eq. (2.2), is equivalent to the variational equation

$$\delta E[\Psi] = 0. \tag{2.3}$$

The approximation of such variational methods consists of the fact that $|\Psi\rangle_{exact}$ is restricted to a set of trial wave functions. As soon as the exact function is not in this set, the minimal solution of eq. (2.3) is an approximation of the exact wave function. The variational method is useful for determining the ground state, since for any trial wave function $|\Psi\rangle$, one can show that the ground state energy will always be a lower bound of a variational calculation [20].

Even though HF theory has the advantage to obtain a mean-field Hamiltonian generated from the many-body system itself, short-range correlations due to free-space two-nucleon force make HF theory not applicable for the bare nucleon-nucleon interaction. Instead, one can use Density Functional Theory (DFT). DFT incorporates the correlations into effective energy-density functionals (EDF).

The SHF approach is a non-relativistic approach regarded in the meantime as reliable and flexible nuclear DFT. Moreover, the SHF apporach is traditionally described by a density-dependent effective interaction, also known as Skyrme energy-density functional or "Skyrme force". There have been many applications of the HF method over the years using different EDFs. Only using density dependent forces it is possible to simultaneously reproduce the binding energies, the radii, and other nuclear properties of light and heavy nuclei all over the nuclear chart [21].

Any mean-field model is built up from a set of single-nucleon wave functions or single-particle (sp) wave functions together with a fractional occupation amplitudes v_α. In order to deal with partially open shells, one augments that by a nuclear pairing scheme [21], which associates an occupation amplitude, v_α with each single-nucleon state φ_α:

$$\{\varphi_\alpha, v_\alpha; \alpha = 1, ..., \Omega\}. \tag{2.4}$$

The occupation amplitude can take values in the interval [0,1]. The complementary non-occupation amplitude is $u_\alpha = \sqrt{1 - v_\alpha^2}$, so that $u_\alpha^2 + v_\alpha^2 = 1$. In the Bardeen–Cooper–Schrieffer (BCS) approximation [22] , the nuclear many-body state is written as follows

$$|\Psi\rangle = \prod_{\alpha>0} (u_\alpha + v_\alpha \hat{a_\alpha} \hat{a_\alpha}^\dagger)|0\rangle, \tag{2.5}$$

where $|0\rangle$ is the vacuum state. This BCS state comprises all the information carried in eq. (2.4). The quantity $\Omega > A$ denotes the size of the pairing-active space. Dynamical degrees of freedom are the single-particle wavefunctions φ_α which yield the mean-field Schrödinger equation and variations with respect to the complementary non-occupation amplitude, u_α yield the pairing equations.

Wavefunctions and occupations amplitudes uniquely define the full one-body density matrix. EDFs such as the Skyrme-energy-density functional are defined in terms of only

a few local densities and currents:

$$\rho_q = \sum_{\alpha\in q} f_\alpha v_\alpha^2 |\varphi_\alpha|^2 \qquad \text{(density)}, \tag{2.6}$$

$$\boldsymbol{s}_q = \sum_{\alpha\in q} f_\alpha v_\alpha^2 \varphi_\alpha^\dagger \hat{\sigma} \varphi_\alpha \qquad \text{(spin density)}, \tag{2.7}$$

$$\boldsymbol{j}_q = \mathrm{Im}\left\{ \sum_{\alpha\in q} f_\alpha v_\alpha^2 \varphi_\alpha^\dagger \bigtriangledown \varphi_\alpha \right\} \qquad \text{(current)}, \tag{2.8}$$

$$\mathbf{J}_q = -i \sum_{\alpha\in q} f_\alpha v_\alpha^2 \varphi_\alpha^\dagger \bigtriangledown \otimes \hat{\sigma} \varphi_\alpha \qquad \text{(spin-orbit density)}, \tag{2.9}$$

$$\tau_q = \sum_{\alpha\in q} f_\alpha v_\alpha^2 |\bigtriangledown \varphi_\alpha|^2 \qquad \text{(kinetic density)}, \tag{2.10}$$

$$\boldsymbol{\tau}_q = -i \sum_{\alpha\in q} f_\alpha v_\alpha^2 \bigtriangledown \varphi_\alpha^\dagger \cdot \bigtriangledown \hat{\sigma} \varphi_\alpha \qquad \text{(kinetic spin-density)}, \tag{2.11}$$

$$\xi_q = \sum_{\alpha\in q} f_\alpha u_\alpha v_\alpha \varphi_{\bar{\alpha}} \varphi_\alpha \qquad \text{(pairing density)}, \tag{2.12}$$

where q labels the nucleon species with $q = p$ for protons and $q = n$ for neutrons. $\varphi_{\bar{\alpha}}$ is the time reversal partner of φ_α. f_α is a phase-space weight which provides a smooth cutoff of the space of single-particle states included in paring. All the expressions are local quantities depending on $\boldsymbol{r}$ and referring to the local wavefunction components $\varphi = \varphi(\boldsymbol{r})$.

The Skyrme potential can be parametrised as [21]

$$\begin{aligned} V_{Sk} = {} & t_0(1 + x_0\hat{P}_\sigma)\delta(\boldsymbol{r}_{12}) + \frac{t_3}{6}(1 + x_3\hat{P}_\sigma)\rho^\gamma(\boldsymbol{r_1})\delta(\boldsymbol{r_{12}}) \\ & + \frac{t_1}{2}(1 + x_1\hat{P}_\sigma)\Big(\delta(\boldsymbol{r}_{12})\hat{\boldsymbol{k}}^2 + \hat{\boldsymbol{k}}^2\delta(\boldsymbol{r}_{12})\Big) + t_2(1 + x_2\hat{P}_\sigma)\hat{\boldsymbol{k}}\delta(\boldsymbol{r}_{12})\hat{\boldsymbol{k}} \\ & - it_4\delta(\boldsymbol{r}_{12})(\hat{\sigma} + \hat{\sigma'}) \cdot (\hat{\boldsymbol{k}'} \times \hat{\boldsymbol{k}}), \end{aligned} \tag{2.13}$$

where the labels in $\boldsymbol{r}_{12} = \boldsymbol{r}_1 - \boldsymbol{r}_2$ refer to particle 1 and 2 and $\hat{P}_\sigma = \frac{1}{2}(1 + \hat{\sigma}_1\hat{\sigma}_2)$ is the spin-exchange operator and the $\hat{\sigma}$ are Pauli spin matrices. The $\hat{k} = -i\bigtriangledown$ are the momentum operators (divided by $\hbar$). Note that the $t_{0,1,2}$ terms in eq. (2.13), correspond to the zero-range limit of a Gogny-type force up to the second order in the derivatives [23, 24]. In addition, t_3 accounts for the three-body force. Nonetheles, in HF calculations of even-even nuclei, as it is the case of our work, this force is equivalent to a two-body density-dependent interaction, where the density dependence is determined by the γ parameter. Eventually, t_4 term accounts for the spin-orbit interaction. The $t_{0,1,2,3,4}$ and

$x_{0,1,2,3}$ force parameters are fitted to nuclear properties solving HF equations. We would like to highlight that in SKYAX, time-odd pieces such as current, spin-density and kinetic spin-density are ignored [9].

Despite the fact that V_{Sk} is not a true interaction [25], eq. (2.13) serves as a generator of the Skyrme interaction functional

$$E_{sk} = \langle \Psi | V_{Sk} | \Psi \rangle. \tag{2.14}$$

The starting point for the SHF approach, as in any DFT, is the total energy which is expressed as follows

$$E_{tot} = E_{kin} + E_{sk} + E_{Coul} + E_{pair} + E_{cm}, \tag{2.15}$$

with kinetic energy

$$E_{kin} = \sum_{q \in p,n} \frac{\hbar^2}{2m_q} \int dV \tau_q, \tag{2.16}$$

where dV is the volume element in the full three-dimensional space. Skyrme energy

$$E = \int dV \Bigg(\frac{b_0}{2}\rho^2 - \frac{b_0'}{2}\sum_q \rho_q^2 + \frac{b_3}{3}\rho^{\gamma+2} - \frac{b_3'}{3}\rho^{\gamma}\sum_q \rho_q^2 - \frac{b_2}{2}\rho\Delta\rho + \frac{b_2'}{2}\sum_q \rho_q \Delta\rho_q$$

$$+ b_1\rho\tau - b_1'\sum_q \rho_q\tau_q - b_4\rho \bigtriangledown \cdot \boldsymbol{J} - b_4'\sum_q \rho_q \bigtriangledown \cdot \boldsymbol{J}_q - c_1\boldsymbol{J}^2 + c_1'\sum_q \boldsymbol{J}_q^2 \Bigg), \tag{2.17}$$

Coulomb energy

$$E_C = \frac{e^2}{2}\int dV dV' \frac{\rho_p(\boldsymbol{r})\rho_p(\boldsymbol{r'})}{|\boldsymbol{r} - \boldsymbol{r'}|} - \int dV \frac{3e^2}{4}\Big(\frac{3}{\pi}\Big)\rho_p^{4/3}, \tag{2.18}$$

where e is the elementary charge with $e^2 = 1.43989 MeV \cdot fm$. The second term in eq. (2.18) is the Slater approximation to the exchange term [26, 27] And pairing energy

$$E_{pair} = \frac{1}{4}\sum_{q \in p,n} V_{pair,q} \int dV |\tilde{\varsigma}_q|^2 \Big[1 - \frac{\rho}{\rho_{0,pair}}\Big], \tag{2.19}$$

where $\rho_{0,pair}$ accounts for the regulation between volume and surface pairing[28].

Despite the fact that the pairing energy is given as a functional, eq. (2.19) is deduced from a density-dependent delta interaction (DDDI) $V_{pair}^{(DDDI)} = \delta(r_1 - r_2)[1 - \rho(r)/\rho_{0,pair}]$. However, DDDI pairing is quite often simplified taking $\rho_{0,pair} \to \infty$, which means that the pairing energy is related to a volume delta interaction (VDI) and thus replacing the surface pairing.

The Skyrme parameters, b_i, are written in terms of the force parameters t_i and x_i as follows:

$$
\begin{aligned}
b_0 =& t_0(1 + \frac{1}{2}x_0), \\
b'_0 =& t_0(\frac{1}{2} + x_0), \\
b_1 =& \frac{1}{4}[t_1(1 + \frac{1}{2}x_0 + t_2(1 + \frac{1}{2}x_2)], \\
b'_1 =& \frac{1}{4}[t_1(\frac{1}{2} + x_0 + t_2(\frac{1}{2} + x_2)], \\
b_2 =& \frac{1}{8}[3t_1(1 + \frac{1}{2}x_1) - t_2(\frac{1}{2} + x_2)], \\
b'_2 =& \frac{1}{8}[3t_1(\frac{1}{2} + x_1) + t_2(1 + \frac{1}{2}x_2)], \\
b_3 =& \frac{1}{4}t_3(1 + \frac{1}{2}x_3), \\
b'_3 =& \frac{1}{4}t_3(\frac{1}{2} + x_3),
\end{aligned}
$$

$$
\begin{aligned}
b_4 =& \frac{1}{2} t_4, \\
b'_4 =& \frac{1}{2} t_4, \\
c_1 =& \eta_{tls} \frac{1}{16} (t_1 x_1 + t_2 x_2), \\
c'_1 =& \eta_{tls} \frac{1}{16} (t_1 - t_2),
\end{aligned} \tag{2.20}
$$

where $\eta_{tls} \in [0, 1]$ controls the contribution from the tensor spin-orbit term. The force definition, see eq. (2.13), fixes the definition of b'_4. In addition, this turns out to be too restrictive for detailed observables and this parameter is usually left as a free parameter.

In this work, we have selected four Skyrme parametrisations:

- SLY4, a Skyrme-like effective interaction usually used to describe neutron stars, supernovae and neutron-rich nuclei is constrained to the pure neutron matter equation-of-state in addition to the standard properties of symmetric infinite nuclear matter in order to have a good behaviour with respect to the isospin degree of freedom [29].

- SKI3 which complements the standard relativistic and non-relativistic effective interactions. Relativistic and non-relativisitic interactions did not predict the same behaviour of the isotope shifts in the Pb [30]. Within the SKI family of parametrisations, SKI3 allows for a $b_4 \neq b'_4 = 0$ value – e.g. in page 479 in Ref.[30]. For the set SKI3, we have imposed the constraint $b \simeq 0$. In this way, we enforce a density dependence of the spin-orbit form factor proportional to $\rho = \rho_p + \rho_n$ as in the relativistic mean field.

- UNEDF0, a nuclear EDF restricted to time-even densities, specially designed to study spherical or axially deformed nuclei. The functional is fitted to reproduce experimental data for 72 nuclei. 11 nuclei are below $A = 66$ while the rest are above $A > 106$, making an emphasis on heavy nuclei. In particular, the fit considers the binding energies of 44 well-deformed even-even nuclei, including the binding energies of the ^{170}Yb and ^{178}Yb isotopes. The remaining 28 selected nuclei are spherical[31].

Table 2.1.: Fitted t_i values for the Skyrme parametrisations used in this work.

Skyrme Force	t_0	t_1	t_2	t_3	t_4
SLY4	-2488.913	486.818	-546.395	13777.000	123.000
SKI3	-1762.880	561.608	-227.0.90	8106.200	188.508
UNEDF0	-1883.688	277.500	607.565	13901.948	250.322
UNEDF1	-2078.328	239.401	1574.243	14263.646	76.736

Table 2.2.: Fitted x_i and b'_4 parameters values for the Skyrme parametrisations used in this work.

Skyrme Force	x_0	x_1	x_2	x_3	b'_4
SLY4	0.834	-0.344	-1.000	1.254	61.500
SKI3	0.30830	-1.17220	-1.09070	1.29260	0.00001
UNEDF0	0.010182022	-1.7786241	-1.6775989	-0.37954858	-91.26040
UNEDF1	0.05430437	-5.0781477	-1.3665705	-0.16116885	71.31652

- UNEDF1,is a subsequent version of UNEDF0, which incorporates an improved description of fission properties of the actinide nuclei. The main achievement of this parametrisation with UNEDF0 is the removal of the center-of-mass correction. UNEDF1 provides a description of global nuclear properties comparable to UNEDF0[32].

In table 2.1 and table 2.2 we list the values of t_i and x_i for each parametrisations, respectively.

2.1.1. Pairing correlations

The mean field approach is specially useful but, in principle, it is only justified when the gap between the highest occupied shell and the first empty level is sizeable. Otherwise, in subshell closures, it is rather easy to have excitations of particle-hole (*ph*) pairs which would lead to more complicated wave-functions than a Slater determinant. Because of that, the HF method is more accurate for the ground state of magical nuclei rather than in other nuclei with a few particles outside the closed shell configuration. These nuclei may show a small deformation in the HF method and have several nearly degenerate levels in the vicinity of the Fermi surface [20].

We are looking for a wave-function that was able to describe the nucleus. The solution

of the corresponding equation led to a transformation from a given sp basis to a better one. The HF method partially takes into account the long-range part of the nuclear interaction as the variational principle is equivalent to the requirement that there are no matrix elements between the ground state and the most simple excitations: the *ph*-excitations. On the other hand, the short-range part of the nuclear interaction is the responsible for particle-particle (*pp*) correlations. The formulation of these *pp* correlations can be done similarly to the *ph* picture by introducing a generalised product of wave-functions conformed of quasi-particles.

The study of pairing correlations allowes one to understand a large number of relevant effects unexplained in the pure HF picture. For example, the spectra of deformed nuclei differ if one observes an even or an odd nuclei. Even-even nuclei have only few collective levels up to, typically $\sim$ 1.5MeV, while the picture is very different for even-odd nuclei, which have many collective and single-particles states in the same energy interval. The former is well described as rotational and vibrational bands, while the latter can be understood using pairing correlations arguments. Another experimental feature that can be explained with pairing correlations is the very well known odd-even effect where the total binding energy of an odd-even nucleus is smaller than the mean value of the binding energies of the two neighbouring even-even nuclei. Also, the moments of inertia of deformed nuclei can be measured from the level structure of rotational bands. Pure sp calculations deviate from experiments by a factor of two whilst the agreement between theory and experiment is rather improved if one includes pairing correlation, leading to a better agreement between both parts.

The coupled mean-field equations are derived by a variation with respect to the sp wave function,

$$\left(\hat{h} + \frac{u_\alpha}{v_\alpha \Delta(r)}\right)\varphi_\alpha = \varepsilon_\alpha \varphi_\alpha, \tag{2.21}$$

$$(\varepsilon_\alpha - \varepsilon_{F,q_\alpha})(u_\alpha^2 - v_\alpha^2) = \Delta_\alpha w_\alpha u_\alpha v_\alpha, \tag{2.22}$$

where $\varepsilon_{F,q}$ stands for the Fermi energy, w_α is the cutoff profile, $\Delta(\mathbf{r})$ is the BCS gap potential, Δ_α is the average sp gap and $\hat{h}$ is the sp hamiltonian. Both eq. (2.21) and eq. (2.22), represent the Hartree-Fock-Bogoliugov equations. However, its solution is rather involved due to the state dependent contribution of the gap potential in eq. (2.21). Therefore, SKYAX omits this last term and deals with the BCS approximation. The solution of the gap equation, eq. (2.22), applies to even-even nuclei which is the common

application of SKYAX and our nuclei of interest. Therefore, we disregard the case of even-odd or odd-even nuclei which require a blocked state with $v_\alpha^2 = 0.5$. Nonetheless, the BCS approximation may lead to unstable solutions[9]. These disadvantages disappear if particle-number projection is applied before the variational derivation of the coupled mean-field equations. A simpler way to approximate particle-number projection is given by the Lipkin-Nogami (LN) scheme. SKYAX use an alternative way to represent the LN scheme that has the same effect, called stabilised pairing, which amounts to direct modification of the gaps,

$$\Delta_\alpha \rightarrow \Delta_\alpha \Big(1 + \frac{E_{stab}^2}{E_{pair,q_\alpha}^2}\Big), \tag{2.23}$$

where E_{stab} is numerical parameter and E_{pair,q_α} the pairing energy associated with the nucleon type of the state α.

SKYAX allows us to select, in the input file, a pairing interaction (VDI or DDDI) and a pairing scheme (BCS or LN scheme) for a given Skyrme parametrisation. However, not all pairing interactions, VDI and DDDI, are allowed to be combined with every Skyrme parametrisations as given by table 2.3. We would like to highlight that the only Skyrme parametrisation that is allowed to work with both VDI and DDDI pairing is SKI3. This is due to the fact that the authors of Ref.[33] tested the predictive power of several Skyrme forces comparing the results obtained for the VDI and DDDI pairing with respect to low lying quadrupole spectra along some chains of isotopes around neutron shell closure $N = 82$. They found that neutron rich isotopes are depend on the change of Skyrme parametrisations and on the adjustment of the pairing interaction [33].

Table 2.3.: List of each type of pairing, VDI or DDDI, supported by each Skyrme parametrisation with its pairing scheme, BCS and LN.

Skyrme Force	VDI		DDDI	
	BCS	LN	BCS	LN
SLY4	Yes	Yes	No	No
SKI3	Yes	Yes	Yes	Yes
UNEDF0	Yes	Yes	No	No
UNEDF1	Yes	Yes	No	No

2.2. Theoretical uncertainties

In this section we estimate one of the theoretical uncertainties of the nuclear properties calculated with SKYAX. The uncertainty related to the precision of the numerical calculations. SKYAX is written in cylindrical coordinates, thus:

$$r = \sqrt{x^2 + y^2}, \qquad z = z. \tag{2.24}$$

The dimension of the axial coordinate-space grid is given by,

$$L_r \times L_z, \tag{2.25}$$

where

$$L_r = d_r N_r, \qquad L_z = d_z N_z. \tag{2.26}$$

On the one hand N_r and N_z are the number of cells defined in the radial and azimutal direction, respectively. On the other hand, d_z and d_r are the cell length defined in the r and z direction, respectively. Both quantities, d_r and d_z, are defined in fm. Before getting into details, fig. 2.1 shows a 2D density plot of the ^{170}Yb isotope in its ground state. As we can see, the shape of the isotope is far away from spherical, thus presenting a permanent quadrupole deformation in its ground state. Consequently, the theoretical uncertainties due to d_r and d_z need to be studied separately.

Figure 2.1.: Ground state density of ^{170}Yb along the $\{r, z\}$-plane.

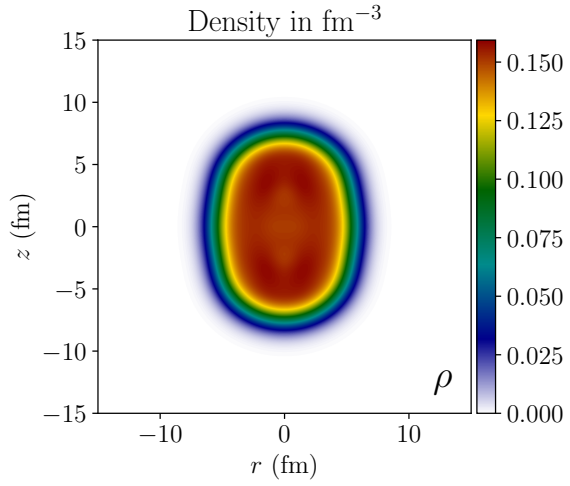

2.2.1. Dimension of the grid

Firstly, we would like to find a suitable box for our calculations. In order to do that, we check how the box lengths, L_r and L_z, affect the convergence of the nuclear properties we aim to determine. We assume that the convergence of nuclear properties does not depend (or depends very smoothly) on the choice of the isotope. Consequently, we have chosen ^{170}Yb for this purpose. Figure 2.2 shows the point-proton radius as a function of the box lengths L_r and L_z. The results have been obtained varying the mesh but an squared box, $L_r = L_z$. Notice that, when $L_r = L_z \geq 22fm$, the point-proton radius, r_p, is almost constant with respect to box length. In contrast, when $L_r = L_z \leq 22fm$ there is an evident dependence on the box length, which is not appropriate to run the calculations. Furthermore, the inset in fig. 2.2 shows that the results are in agreement up to $2 \cdot 10^{-4} fm$ for the $30fm \leq L_z(L_r) \leq 45fm$ range, the precision is about $2 \cdot 10^{-4} fm$ with an overall error of, $\varepsilon^{(L)} = \pm 10^{-4} fm$.

We repeat the same procedure for R_{p4} in fig. 2.3 which shows a steeper evolution of R_{p4} in comparison to R_p. However, we would like to emphasise that the dependence of R_{p4} with respect to the box size is very small for $L_r(L_z) \geq 25fm$. In the restricted zone, $30fm \leq L_r(L_z) \leq 36fm$, the uncertainty in R_{p4} is of the same order as in R_p,

Figure 2.2.: Rms point-proton radius, R_p as a function of box length of ^{170}Yb isotope. We have selected the same value for L_z and L_r (squared box). In addition, each value has been computed keeping d_z and d_r (cell lengths) constant and varying the number of cells, N_z and N_r, inside the squared-box. Red line indicates $d_r = d_z = 0.6fm$, blue line $d_r = d_z = 0.7fm$, green line $d_r = d_z = 0.8fm$, cyan line indicates $d_r = d_z = 0.9fm$ and violet line $d_r = d_z = 1.0fm$.

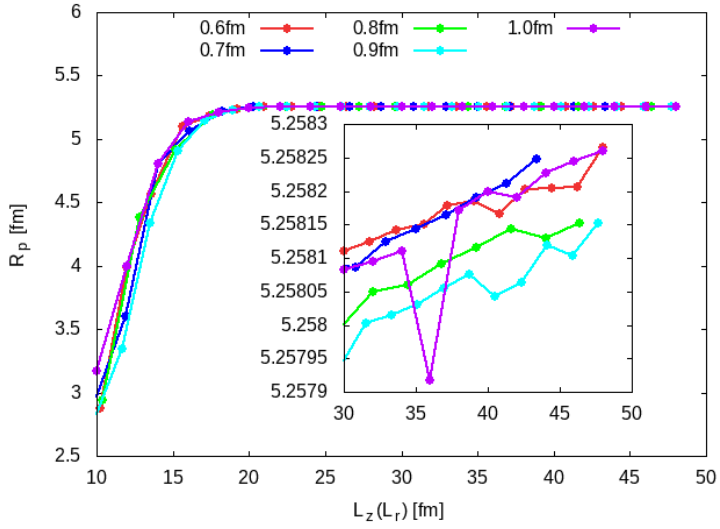

Figure 2.3.: Fourth moment point radius, R_p^4, as a function of box length of ^{170}Yb isotope. Same color code as in fig. 2.2

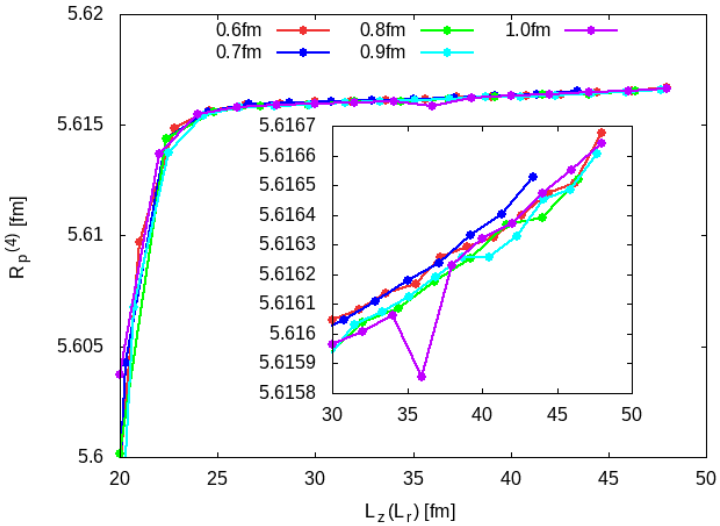

thus $\varepsilon_L^{(4)} = 10^{-4} fm$. Thus we shall limit the calculations of R_{p4} inside of the restricted range in order to achieve this level of precision. In conclusion, all nuclear properties show an uncertainty with the box length of about $10^{-4} fm$. In the following, we use $L_r = L_z = 32 fm$ box.

2.2.2. Optimising mesh parameters

Now we would like to study the theoretical uncertainty of the nuclear properties when we vary the number of cells, N_r and N_z, in the grid and the minimum size of the mesh, defined by d_r and d_z, but keeping the total box dimension constant, $32 fm \times 32 fm$ as we found previously. Figures 2.4 and 2.5, show the dependence with respect to the mesh parameters, d_r and d_z. Figure 2.4 highlights that the computed R_p values are very similar for $d_r = 0.6, 0.7, 0.8, 0.9 fm$. The case is quite the opposite for $d_r = 1.0 fm$ and $d_r = 1.1 fm$ which lead to different R_p values. Inside the zoomed region we spot a quite soften dependence of R_p with respect d_r and d_z, more precisely for $d_z = 0.4 fm$ to $d_z = 0.8 fm$ and $d_r = 0.6 fm$ to $d_r = 0.9 fm$, leading to an uncertainty about $\varepsilon_{R_p}^{(M)} = \pm 10^{-4} fm$.
Figure 2.5 highlights that the computed R_{p4} values are very similar for $d_r = 0.6, 0.7$ $, 0.8, 0.9 fm$. The case is quite the opposite for $d_r = 1.0 fm$ and $d_r = 1.1 fm$ which lead to different R_{p4} values. In the inset figure we spot a quite soften dependence of R_{p4} with respect d_r and d_z, more precisely for $d_z = 0.4 fm$ to $d_z = 0.8 fm$ and $d_r = 0.6 fm$ to $d_r = 0.9 fm$, leading to an uncertainty about $\varepsilon_{R_{p4}}^{(M)} = \pm 10^{-4} fm$.

Figure 2.4.: Rms point-proton radius as a function of mesh d_z parameter. Calculations computed with different mesh d_r parameter and varying the number of cells, N_r and N_z, so as to keep the box dimension constant: $32fm \times 32fm$. A zoom in has been included to have a better resolution inside the converged zone.

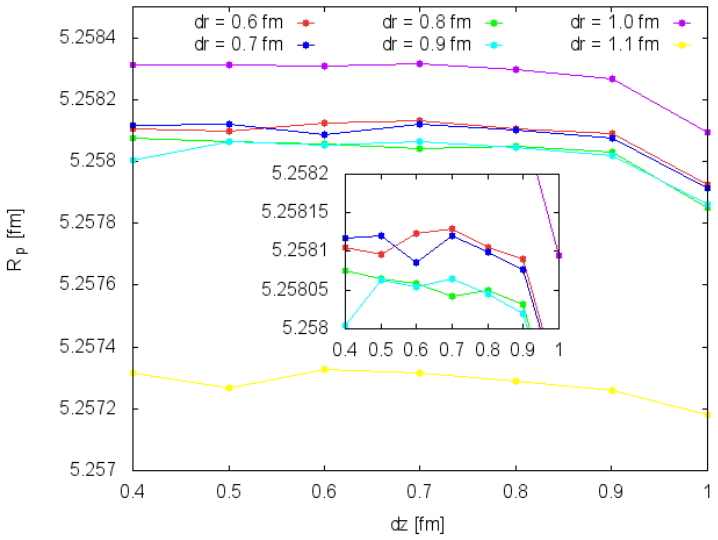

The error due to code's resolution in both nuclear properties are calculated as follows

$$\varepsilon_k^{(C)} = \sqrt{\varepsilon_k^{(M)^2} + \varepsilon_k^{(L)^2}}, \tag{2.27}$$

where $k = R_p, R_{p4}$ Since uncertainties in the dimension of the grid and the mesh are the same for both nuclear properties we shall assign the same name for the theoretical uncertainty, see eq. (2.27). The uncertainties are listed in table 2.4.

Table 2.4.: Mesh, dimension of the grid and theoretical uncertainties associated to both R_p and R_{p4} nuclear quantities.

$\varepsilon_k^{(L)}\ [fm]$	$\varepsilon_k^{(M)}\ [fm]$	$\varepsilon_k^{(C)}\ [fm]$
10^{-4}	10^{-4}	$1,4 \cdot 10^{-4}$

We would like to note that, despite the fact that reducing the mesh parameters and increasing the number of cells lead to a better resolution of the results, this improvement was at expense of a higher computational time. As a consequence, we have chosen suitable values of d_r, d_z, N_r and N_z that are compatible both with a reasonable computational time and the best precision. As mentioned in [9], a good compromise with both computational time and precision is reached for $d_r, d_z = 0.7fm$. Four our purposes,

Figure 2.5.: Fourth moment point-proton radius, R_{p4}, as a function of mesh d_z parameter. Same details as in fig. 2.4.

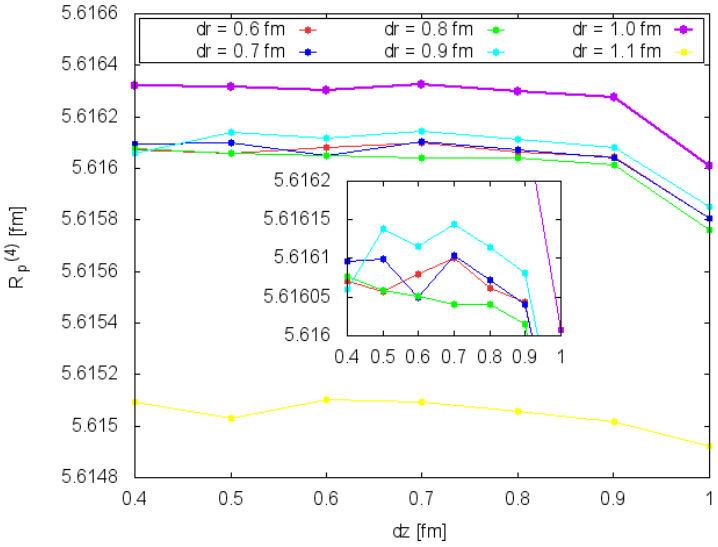

$d_r = d_z = 0.7fm$ and $L_r = L_z = 32fm$ to compute the nuclear properties of the five Yb isotopes.

In the forthcoming section we present the nuclear properties obtained with SKYAX for different Skyrme parametrisations, pairing interactions and pairing schemes. In addition to the uncertainty due to the code's precision, we define a new uncertainty due to the pairing interaction. Moreover, both sources of uncertainty shall be propagated into King's plots to study possible non-linearities and whether they can be due to nuclear uncertainties.

3. Results

In this chapter we present a detailed analysis of the main results obtained in this thesis. The structure of this chapter follows the steps represented in fig. 3.1. First, we use SKYAX to extract the nuclear quantities evaluated in section 2.1 for neighbouring even-even Yb isotopes with zero nuclear spin: ^{A}Yb where $A \in \{168, 170, 172, 174, 176\}$. From these results we obtain the nuclear properties of interest discussed in chapter 1 such as the differential squared charge radius, $\delta\langle r^2\rangle$, and the differential fourth order charge radius, $\delta\langle r^4\rangle$. In addition, all these nuclear properties have an associated theoretical error. One

Figure 3.1.: Flow diagram describing the steps followed to calculate deviations from linearity in the IS of Yb.

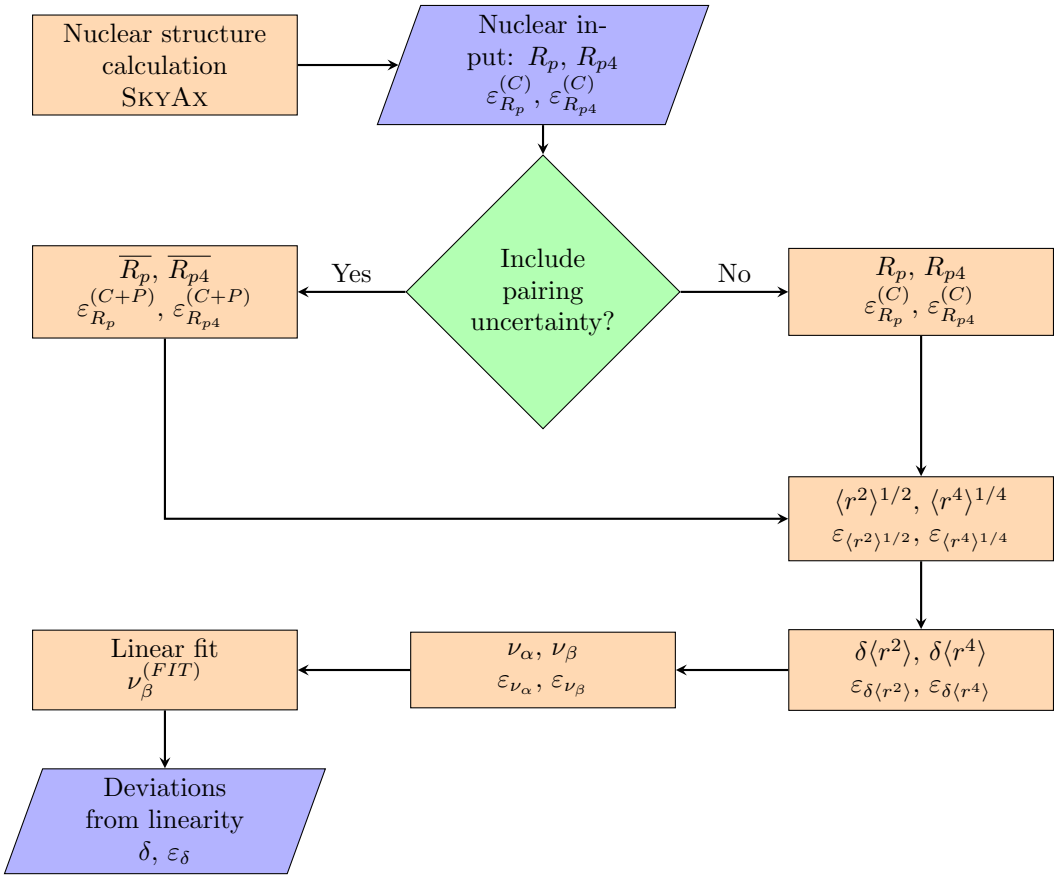

source of theoretical error is the code's precision. The second source of theoretical uncertainty takes into account the uncertainty due to different pairing schemes using the same Skyrme parametrisation. With the nuclear properties and its theoretical uncertainties we determine the theoretical frequency shifts for both α and β transitions and their respective uncertainties. Eventually we calculate the deviation from linearity and its theoretical uncertainty.

Since SKI3 is the only Skyrme parametrisation that incorporates both pairing interactions, VDI and DDDI, we obtain 4 values of the same nuclear property for a given isotope. The other Skyrme parametrisations are restricted to VDI only, thus resulting in 2 values of the same nuclear property for each parametrisation. Consequently, for a given isotope we obtain 10 different values of the same nuclear property. For the sake of simplicity, we only present results coming from SLY4 Skyrme parametrisation. The rest can be found in appendices B to F.

3.1. Point-proton and fourth moment point-proton radii with theoretical uncertainties

3.1.1. Results with the code's uncertainty

In this subsection, we present the point-proton radius, R_p, and the fourth moment point-proton radius, R_{p4}, for each Yb isotope of interest. Before getting into details, we would like to remark that the code's precision calculated in the previous chapter is the same for both R_p and R_{p4}, $\varepsilon^{(C)} = 1.4 \cdot 10^{-4} fm$. In table 3.1 we present the results obtained using the SLY4 parametrisation. When we consider the pairing schemes separately, the

Table 3.1.: Point-proton radius obtained with SKYAX using the SLY4 Skyrme parametrisation and different pairing schemes (BCS or LN). The uncertainties within this table are due to the code's precision.

Isotope	$R_p\ [fm]$		$R_{p4}\ [fm]$	
	BCS	LN	BCS	LN
^{168}Yb	5.24220(14)	5.24252(14)	5.59947(14)	5.59996(14)
^{170}Yb	5.25812(14)	5.25879(14)	5.61610(14)	5.61716(14)
^{172}Yb	5.27116(14)	5.27120(14)	5.62845(14)	5.62867(14)
^{174}Yb	5.28232(14)	5.28218(14)	5.63868(14)	5.63795(14)
^{176}Yb	5.29344(14)	5.29282(14)	5.64644(14)	5.63794(14)

total theoretical uncertainty, $\varepsilon^{(T)}$, is given by the code's precision, $\varepsilon^{(C)}$. Consequently, $\varepsilon^{(T)}_{R_p} = \varepsilon^{(T)}_{R_{p4}} = 1.4 \cdot 10^{-4} fm$ for both point-proton radii. In the following subsection we introduce a different type of uncertainty, extracted from the difference between both pairing schemes for a given pairing interaction, namely the pairing uncertainty.

3.1.2. Results with pairing uncertainty

When we take into account both pairing schemes (BCS+LN), the nuclear properties of interest are calculated taking the mean value between both pairing schemes,

$$\overline{X} = \frac{X(BCS) + X(LN)}{2}, \tag{3.1}$$

where $X \in \{R_p, R_{p4}, \langle r^2 \rangle^{1/2}, \langle r^4 \rangle^{1/4}, \delta\langle r^2 \rangle, \delta\langle r^4 \rangle\}$. In order to characterise the pairing uncertainty for the point-proton radii we take the absolute difference between the results obtained with the two pairing schemes:

$$\varepsilon^{(P)}_X = \frac{|X_{(BCS)} - X_{(LN)}|}{2}. \tag{3.2}$$

However, we highlight that X in eq. (3.2) refers only to the point-proton radii, R_p and R_{p4}. This notation is maintained throughout the rest of this work. For the point-proton radii, this uncertainty is combined with the code's precision so that the overall theoretical uncertainty is calculated as follows

$$\varepsilon^{(T)}_X = \sqrt{\left(\varepsilon^{(C)}\right)^2 + \left(\varepsilon^{(P)}_X\right)^2}. \tag{3.3}$$

The uncertainties related to the remaining nuclear quantities are calculated by means of the error propagation of eq. (3.3), and the value of the nuclear quantities are computed in virtue of eq. (3.1) The total theoretical uncertainty has three possible outcomes:

- $\varepsilon^{(C)} >> \varepsilon^{(P)}_X$, the error due to the code's precision is much larger than the pairing uncertainty. As a consequence, the total theoretical uncertainty is dominated by the code's precision, $\varepsilon^{(T)}_X \sim \varepsilon^{(C)}$.
- $\varepsilon^{(C)} << \varepsilon^{(P)}_X$, the error due to the code's precision is much smaller than the pairing uncertainty, which dominates the total theoretical uncertainty, $\varepsilon^{(T)}_X \sim \varepsilon^{(P)}_X$.
- $\varepsilon^{(C)} \simeq \varepsilon^{(P)}_X$, the code's precision and the pairing uncertainty are of the same order.

Table 3.2 lists the point-proton radii, R_p and R_{p4}, obtained in virtue of eqs. (3.1) to (3.3). We highlight that the introduction of the pairing uncertainty has, in general, a noticeable impact in the total theoretical uncertainty. In first place, the point-proton radius total

Table 3.2.: Point-proton radius, $\overline{R_p}$ and fourth moment point-proton radius, $\overline{R_{p4}}$, with theoretical error including the pairing uncertainty and code's precision.

Isotope	$\overline{R_p}\ [fm]$	$\overline{R_{p4}}\ [fm]$
^{168}Yb	5.24236(21)	5.59971(28)
^{170}Yb	5.25845(36)	5.61663(55)
^{172}Yb	5.27118(14)	5.62856(18)
^{174}Yb	5.28225(16)	5.63832(39)
^{176}Yb	5.29313(34)	5.64608(39)

uncertainty is, in general, governed by the difference between both pairing schemes, thus $\varepsilon^{(T)}_{R_p} \sim \varepsilon^{(P)}_{R_p}$. In comparison, the theoretical uncertainty when we include the pairing uncertainty is 2.5 times greater, at most, than when we only considered the code's precision as the only source of theoretical uncertainty, see table 3.1. Nonetheless, there are two exceptions: the ^{172}Yb isotope has a theoretical uncertainty that is equal to the code's precision, $\varepsilon^{(T)}_{R_p} \sim \varepsilon^{(C)}$, due to the fact that the difference between both pairing schemes is $1.4 \cdot 10^{-4} fm$, which greater than the code's precision. Meanwhile, the ^{174}Yb isotope both the pairing and the code's uncertainty have similar values. In appendix B.1 we gathered the point-proton radius values with the remaining Skyrme forces. For all the remaining Skyrme forces, , see tables B.1 to B.3, the inclusion of the pairing uncertainty is, in general, larger than the code's precision, leading to a noticeable impact on the point-proton radius theoretical uncertainty. In some particular cases, the pairing uncertainty is smaller than the code's precision, meaning that the relative difference between both pairing schemes is smaller than the actual precision of the code. However, this special does not affect the same isotope when we change the Skyrme force. For example, for UNEDF0, see table B.3, ^{168}Yb and ^{174}Yb isotopes have a smaller pairing uncertainty than the code's precision. Meanwhile, for SkI3 with VDI pairing interaction, see table B.1, is the ^{170}Yb which has a smaller discrepancy between pairing schemes than the code's precision. The same happens with the fourth moment. Typically, the inclusion of pairing uncertainty leads to larger R_{p4} theoretical uncertainties than when we treat both pairing schemes separately. The R_{p4} values for the remaining Skyrme forces are listed in appendix B.2.

In the following sections we derive the nuclear properties of interest for the characterisation of the Yb^+ IS with theoretical uncertainties.

3.2. Charge radius

The squared rms charge radius of a given Yb isotope is given by eq. (1.5):

$$\langle r^2 \rangle = R_p^2 + \langle r_p^2 \rangle + \langle r_p^2 \rangle_{so} + \frac{N}{Z}\Big(\langle r_n^2 \rangle + \langle r_n^2 \rangle_{so} \Big). \tag{3.4}$$

The numerical values of the electromagnetic mean-square radius of the proton and neutron used within this work are taken from [34], and their values are $\langle r_p^2 \rangle = 0.7071(7) fm^2$ and $\langle r_n^2 \rangle = -0.1161(22) fm^2$, respectively. In this work we take the approximation of neglecting both proton and neutron spin-orbit corrections. As a consequence, the rms charge radius is written as follows

$$\langle r^2 \rangle^{1/2} = \sqrt{R_p^2 + \langle r_p \rangle^2 + \frac{N}{Z} \langle r_n \rangle^2}. \tag{3.5}$$

However, nuclear correlations lead to complex spin-orbit corrections to charge radii [15] that can amount up to $0.01 fm$ in some nuclei [35]. In particular, some calculations suggest that spin-orbit contributions can lead to a $0.001 fm$ correction of the ^{176}Yb rms charge radius [15]. Therefore, our results should be taken as an approximation.

All theoretical uncertainties, regarding the nuclear properties, are calculated assuming that there are no correlations between the variables that define each nuclear property. We use the statistical standard deviation formula taking into account independent variables [36, 37]. Therefore, the theoretical rms charge radius uncertainty is given by

$$\begin{aligned} \varepsilon_{\langle r^2 \rangle^{1/2}} &= \sqrt{\left(\frac{\partial \langle r^2 \rangle^{1/2}}{\partial R_p} \varepsilon_{R_p}^{(T)} \right)^2 + \left(\frac{\partial \langle r^2 \rangle^{1/2}}{\partial \langle r_n^2 \rangle} \varepsilon_{\langle r_n^2 \rangle} \right)^2 + \left(\frac{\partial \langle r^2 \rangle^{1/2}}{\partial \langle r_p^2 \rangle} \varepsilon_{\langle r_p^2 \rangle} \right)^2} \\ &= \frac{\sqrt{(2R_p \varepsilon_{R_p}^{(T)})^2 + (\frac{N}{Z} \varepsilon_{\langle r_n^2 \rangle})^2 + (\varepsilon_{\langle r_p^2 \rangle})^2}}{2\langle r^2 \rangle^{1/2}}, \end{aligned} \tag{3.6}$$

where $\varepsilon_{R_p}^{(T)} = \varepsilon^{(C)}$ if we consider pairing schemes independently, see the second and third column in Table 3.3. In this case, the dominant term in eq. (3.6) is due to the error propagation of $\varepsilon_{\langle r_n^2 \rangle}$. This term is one order of magnitude larger than the other terms in eq. (3.6). However, this dominant term is nearly constant over the isotopic chain considered in this work, about $33 \cdot 10^{-5} fm$. The ascending trend in the second digit of the uncertainty is justified by the increase in R_p as we increase the number of neutrons in the Yb isotopic chain. On the other hand, when we include the pairing uncertainty, see the last column in table 3.3, the conclusion is different. In some cases, the first and the second terms of eq. (3.6) has the same nearly the same value $\simeq 33 \cdot 10^{-5} fm$. This is the case of ^{168}Yb, ^{170}Yb and ^{176}Yb isotopes. However, for ^{172}Yb and ^{174}Yb isotopes the main

Table 3.3.: Theoretical rms charge radius obtained with the SLY4 Skyrme parametrisation. The second and third columns are obtained using BCS and LN pairing schemes, respectively. The fourth column takes the mean value of both pairing schemes.

Isotope	$\langle r^2 \rangle^{1/2}$ $[fm]$		$\overline{\langle r^2 \rangle^{1/2}}$ $[fm]$
	BCS	LN	BCS+LN
^{168}Yb	5.29389(33)	5.29421(33)	5.29405(37)
^{170}Yb	5.30934(33)	5.31000(33)	5.30967(47)
^{172}Yb	5.32194(34)	5.32198(34)	5.32196(34)
^{174}Yb	5.33269(34)	5.33254(34)	5.33262(35)
^{176}Yb	5.34339(35)	5.34278(35)	5.34308(46)

source of uncertainty is the second term in eq. (3.6) because the theoretical uncertainty in R_p is nearly the code's precision.

In the following subsection we compute the differential squared charge radius for consecutive neighbouring Yb isotopes, including the corresponding error. This quantity is directly related to the King's plot.

3.3. Differential squared charge radius

The differential squared charge radius between two Yb isotopes, namely ^{A}Yb and $^{A+2}$Yb is given by eq. (1.4):

$$\delta\langle r^2 \rangle_{ji} = \langle r^2 \rangle_j - \langle r^2 \rangle_i.$$

where $i = A + 2$ and $j = A$, leading to $i = j + 2$. Substituting eq. (3.5) into eq. (1.4) we can obtain the differential squared charge radius in terms of R_p, $\langle r_n^2 \rangle$ and $\langle r_p^2 \rangle$:

$$\delta\langle r^2 \rangle_{ji} = R_{p,j}^2 - R_{p,i}^2 - \frac{2}{Z}\langle r_n^2 \rangle. \tag{3.7}$$

Thus, eq. (3.7) depends on the differential squared point-proton radius between two consecutive even-even Yb isotopes and, since we are dealing with Yb isotopes ($Z = 70$), it also has a small $-1/35$ dependence with $\langle r_n^2 \rangle$. The intrinsic proton dependence is cancelled out since it does not vary between different isotopes. The corresponding un-

Table 3.4.: Theoretical differential squared charge radii obtained using the SLY4 Skyrme parametrisation. Columns shows results for different pairing schemes as in table 3.3.

Yb isotope pair	$\delta\langle r^2\rangle_{ji}\ [fm^2]$		$\overline{\delta\langle r^2\rangle_{ji}}\ [fm^2]$
(j,i)	BCS	LN	BCS+LN
(168,170)	-0.1639(21)	-0.1675(21)	-0.1657(44)
(170,172)	-0.1339(21)	-0.1274(21)	-0.1307(41)
(172,174)	-0.1145(21)	-0.1125(21)	-0.1135(26)
(174,176)	-0.1142(21)	-0.1092(21)	-0.1117(40)

certainty is given by

$$\varepsilon_{\delta\langle r^2\rangle} = \sqrt{\left(\frac{\partial\delta\langle r^2\rangle_{ji}}{\partial R_{p,i}}\varepsilon^{(T)}_{p,i}\right)^2 + \left(\frac{\partial\delta\langle r^2\rangle_{ji}}{\partial R_{p,j}}\varepsilon^{(T)}_{p,j}\right)^2 + \left(\frac{\partial\delta\langle r^2\rangle_{ji}}{\partial\langle r^2_n\rangle}\varepsilon_{\langle r^2_n\rangle}\right)^2} =$$

$$= 2\sqrt{(R_{p,j}\varepsilon^{(T)}_{p,j})^2 + (R_{p,i}\varepsilon^{(T)}_{p,i})^2 + (\varepsilon_{\langle r^2_n\rangle}/Z)^2}. \tag{3.8}$$

Table 3.4 presents the results for $\delta\langle r^2\rangle_{ji}$. In the second and the third columns, we take the pairing schemes independently so that the propagated theoretical uncertainty in R_p is due the code's precision solely. In this case, the first two terms of eq. (3.8) account for 85% to 99% of $\varepsilon_{\delta\langle r^2\rangle}$, and the contribution of $\varepsilon_{\langle r^2_n\rangle}$ is tiny in comparison due to the $1/Z$ factor. The propagated error in the first two columns has a constant value over different isotope pairs as the product $R_p\varepsilon_{R_p}$ does not vary (up to the third non-zero digit) between them. The relative uncertainty is about 1% to 2%. In the fourth column of table 3.4 we take both pairing schemes, including the pairing uncertainty into $\varepsilon^{(T)}_p$. In this scenario, the relative uncertainty in $\delta\langle r^2\rangle_{ji}$ is about 2.5% to 3.6%, nearly 2 times bigger than when we consider the pairing schemes independently. This is because the pairing uncertainty is typically larger than the code's precision. However, the $(172, 174)$ Yb isotope pair is an exception. For this isotope pair, the pairing uncertainty is similar to the code's precision and, consequently, in this case the propagated uncertainty in $\delta\langle r^2\rangle$ is similar to when we consider the pairing schemes independently.

Here we note that a recent extraction from the deuteron points to a slightly smaller value of the electromagnetic mean-square radius of the neutron, $\langle r^2_n\rangle = -0.106^{+0.007}_{-0.005} fm^2$ [38] . Therefore, different values of $\langle r^2_n\rangle$ could lead to discrepancies in $\delta\langle r^2\rangle$, since eq. (3.7) depends on this value. The actual discrepancy between the results obtained in [34] and [38] are of $\sim 10\%$, resulting in a $\sim 0.1\%$ discrepancy in $\delta\langle r^2\rangle$. Even if we had not included the additional pairing uncertainty, the main source of uncertainty in $\delta\langle r^2\rangle$ would still be

the first two terms in eq. (3.8).

3.4. Differential fourth moment charge radius

The differential fourth moment charge radius between to neighbouring even-even Yb isotopes, namely ^{j}Yb and ^{i}Yb, where $j = A$ and $i = A + 2$ is given by eq. (1.20):

$$\delta\langle r^4\rangle_{ji} = \langle r^4\rangle_j - \langle r^4\rangle_i.$$

The fourth moment charge radius $\langle r^4\rangle$ is related to the fourth moment point-proton radius R_{p4} adding corrective terms [39]. However, we neglect spin-orbit corrections for consistency with the approximation taken for the charge radius, see eq. (1.5). Consequently, the expression for $\langle r^4\rangle$ is given as follow

$$\langle r^4\rangle = (R_{p4})^4 + \frac{10}{3}\left[\langle r_p^2\rangle R_p^2 + \langle r_p^4\rangle + \frac{N}{Z}\left(\langle r_n^2\rangle R_n^2 + \langle r_n^4\rangle\right)\right], \tag{3.9}$$

where $\langle r^4_{p(n)}\rangle$, is the fourth moment of charge distribution of the proton (neutron) and R_n is the point-neutron radius. Therefore, the differential fourth order charge radius is given by

$$\delta\langle r^4\rangle_{ji} = \left(R_{p4,j}\right)^4 - \left(R_{p4,i}\right)^4 + \frac{10}{3}\left[\langle r_p^2\rangle\left(R_{p,j}^2 - R_{p,i}^2\right) + \frac{\langle r_n^2\rangle}{Z}\left(NR_{n,i}^2 - (N+2)R_{n,j}^2\right) - \frac{2}{Z}\langle r_n^4\rangle\right]. \tag{3.10}$$

Table 3.5.: Theoretical differential fourth order charge radii obtained with the SLY4 Skyrme parametrisation. Columns show the results for different pairing schemes as in table 3.3.

Yb isotope pair	$\delta\langle r^4\rangle_{ji}$ $[fm^4]$		$\overline{\delta\langle r^4\rangle_{ji}}$ $[fm^4]$
(j,i)	BCS	LN	BCS+LN
(168,170)	-11.74(14)	-12.14(14)	-11.94(43)
(170,172)	-8.78(14)	-8.18(14)	-8.48(41)
(172,174)	-7.32(14)	-6.64(14)	-6.98(31)
(174,176)	-5.57(14)	-5.58(14)	-5.58(40)

Nonetheless, in this work we neglect the corrective terms inside the bracket of eq. (3.10), as a first approximation. Consequently, eq. (3.10) reduces to

$$\delta\langle r^4\rangle_{ji} \simeq \left(R_{p4,j}\right)^4 - \left(R_{p4,i}\right)^4, \tag{3.11}$$

and its uncertainty is given by

$$\begin{aligned}\varepsilon_{\delta\langle r^4\rangle} &= \sqrt{\left(\frac{\partial\delta\langle r^4\rangle_{ji}}{\partial R_{p4,j}}\varepsilon^{(T)}_{p4,j}\right)^2 + \left(\frac{\partial\delta\langle r^4\rangle_{ji}}{\partial R_{p4,i}}\varepsilon^{(T)}_{p4,i}\right)^2} = \\ &= 4\sqrt{\left(\left(R_{p4,j}\right)^3\varepsilon^{(T)}_{p4,j}\right)^2 + \left(\left(R_{p4,i}\right)^3\varepsilon^{(T)}_{p4,i}\right)^2}.\end{aligned} \tag{3.12}$$

Table 3.5 presents the differential fourth moment charge radii of even-even neighbouring Yb isotopes using the SLY4 Skyrme parametrisation. In the second and third columns, we consider the BCS and LN pairing schemes independently and the theoretical uncertainty in the fourth moment point-proton radius is given by the code's precision. In this case, the propagated uncertainty $\varepsilon_{\delta\langle r^4\rangle}$ has a constant value across the isotope pairs with a relative uncertainty about 1% to 2%. The last column in table 3.5 takes both pairing schemes. In this case, the propagated uncertainty is, typically, 2.5 times larger than when we consider the pairing schemes independently, and it is not constant across the isotope pairs due to the inclusion of the pairing uncertainty in $\varepsilon^{(T)}_{R_{p4}}$, see eq. (3.3). The relative error is about 3% to 7%. Nonetheless, the impact of the corrective terms in eq. (3.10) are of the order of $0.3fm^4$ for the $(170, 172)$ isotope pair, which is of the same order of the uncertainty in R_{p4} when we compute the two pairing schemes, see fourth column of table 3.5.

In the forthcoming section we calculate frequency shifts of interest, $\nu_{\alpha,ji}$ and $\nu_{\beta,ji}$ with theoretical uncertainties. With these, we study the King's relation and the inclusion of NL terms, as well as the impact of theoretical uncertainties.

3.5. King's Plot with theoretical uncertainties

Here we calculate the frequency shifts of both α and β transitions of Yb^+ in addition to their theoretical uncertainties. For simplicity, we only show in the main text the results obtained using the SLY4 Skyrme parametrisation. The remaining plots using other Skyrme functionals can be found in Appendix C.

In table 3.6 we list all the necessary atomic quantities to compute the frequency shifts for the α and β transitions of the Yb^+ ion. There is a choice of different constants depending on the many-body schemes. For example, in Ref.[5] they calculate F as a leading

Table 3.6.: Atomic parameters for α and β transitions. No error is assumed in the calculation of these quantities taken from Refs.[5, 8].

K_α	$[GHz \cdot u]$[5]	-1678.3
K_β	$[GHz \cdot u]$[5]	-1638.5
$K_{\beta\alpha}$	$[GHz \cdot u]$[5]	77.8974
F_α	$[GHz/fm^2]$[8]	-17.6035
F_β	$[GHz/fm^2]$[8]	-18.0028
$F_{\beta\alpha}$	[8]	1.0227
$G_\alpha^{(2)}$	$[GHz/fm^4]$[8]	0.02853
$G_\beta^{(2)}$	$[GHz/fm^4]$[8]	0.02853
$G_{\beta\alpha}^{(2)}$	$[kHz/fm^4]$[8]	-647.15
$G_\alpha^{(4)}$	$[GHz/fm^4]$[8]	0.01308
$G_\beta^{(4)}$	$[GHz/fm^4]$[8]	0.01337
$G_{\beta\alpha}^{(4)}$	$[kHz/fm^4]$[8]	-6.6935

term of the Seltzer moment expansion at the origin for the total electron density and then they use partial derivatives of the FS to to calculate $G^{(2)}$ and $G^{(4)}$. This procedure is done for configurational interaction method and MBPT many-body perturbation theory to calculate the atomic quantities. Furthermore, in Ref.[8] they use Brueckner orbitals and the random phase approximation method to calculate F and $G^{(4)}$, and the perturbation theory to find $G^{(2)}$. In this work, we use the values of K_α, K_β, and $K_{\beta\alpha}$ from [5], since these quantities are only computed in there. We take the other atomic quantities from [8] because they provide four digits in $G^{(2)}$ and $G^{(4)}$ to avoid the effect of rounding on the nonlinearity.

The frequency shifts, $m\nu_{\alpha,ji}$ and $m\nu_{\beta,ji}$, are computed in virtue of eqs. (1.18) and (1.19):

$$m\nu_{\alpha,ji} = K_\alpha + F_\alpha m\delta\langle r^2\rangle_{ji} + G_\alpha^{(2)} m\left[\delta\langle r^2\rangle_{ji}\right]^2 + G_\alpha^{(4)} m\delta\langle r^4\rangle_{ji},$$

$$m\nu_{\beta,ji} = K_\beta + F_\beta m\delta\langle r^2\rangle_{ji} + G_\beta^{(2)} m\left[\delta\langle r^2\rangle_{ji}\right]^2 + G_\beta^{(4)} m\delta\langle r^4\rangle_{ji},$$

In order to calculate the frequency-shifts uncertainties we assume the nuclear properties μ_{ji}, $\delta\langle r^2\rangle_{ji}$ and $\delta\langle r^4\rangle_{ji}$ as independent variables. In addition, we assume that all atomic quantities carry no error, see table 3.6. Therefore, the propagated uncertainties for both frequency shifts, namely $\varepsilon_{\alpha,ji}$ and $\varepsilon_{\beta,ji}$, are given by

Table 3.7.: Measured inverse-mass differences, μ_{ji}, [5].

Isotope pair (j,i)	μ_{ji} $[10^{-6}u^{-1}]$
(168, 170)	70.113 698(46)
(170, 172)	68.506 890 50(63)
(172, 174)	66.958 651 95(64)
(174, 176)	65.474 078 21(65)

$$\varepsilon_{\omega,ji} = \sqrt{\left(\frac{\partial(m\nu_\omega)}{\partial m\delta\langle r^2\rangle_{ji}}\right)^2 \varepsilon^2_{m\delta\langle r^2\rangle_{ji}} + \left(\frac{\partial(m\nu_\omega)}{\partial m\delta\langle r^4\rangle_{ji}}\right)^2 \varepsilon^2_{m\delta\langle r^4\rangle_{ji}}} =$$

$$= \sqrt{\left(F_\omega + 2G^{(2)}_\omega \delta\langle r^2\rangle_{ji}\right)^2 \varepsilon^2_{m\delta\langle r^2\rangle_{ji}} + \left(G^{(4)}_\omega\right)^2 \varepsilon^2_{m\delta\langle r^4\rangle_{ji}}}, \quad \omega = \alpha, \beta, \tag{3.13}$$

where the uncertainties associated to the modified differential squared charge radius, $\varepsilon_{m\delta\langle r^2\rangle_{ji}}$, and modified differential fourth moment charge radius, $\varepsilon_{m\delta\langle r^4\rangle_{ji}}$, are obtained as

$$\varepsilon_{m\mathcal{Q}} = \sqrt{\left(\frac{\partial m\mathcal{Q}}{\partial \mathcal{Q}}\right)^2 \varepsilon^2_{\mathcal{Q}} + \left(\frac{\partial m\mathcal{Q}}{\partial \mu_{ji}}\right)^2 \varepsilon^2_{\mu_{ji}}} = m\mathcal{Q}\sqrt{\left(\frac{\varepsilon_{\mathcal{Q}}}{\mathcal{Q}}\right)^2 + \left(\frac{\varepsilon_{\mu_{ji}}}{\mu_{ji}}\right)^2}, \tag{3.14}$$

with $\mathcal{Q} = \delta\langle r^2\rangle_{ji}, \delta\langle r^4\rangle_{ji}$. The experimental inverse-mass differences, in addition to its experimental uncertainty, are listed in table 3.7.

Figure 3.2 shows the standard King's plot between the modified frequency shifts, $m\nu_\alpha$ and $m\nu_\beta$ using BCS (left panel) and LN (right panel) pairing schemes. In both panels, the red line is obtained from a linear fit to the blue points, which, in principle, represents King's linearity, see eq. (1.16). The theoretical uncertainties, $\varepsilon_{\alpha,ji}$ and $\varepsilon_{\beta,ji}$, are about 1% of the calculated theoretical frequency shifts. These large theoretical uncertainties are also found with other parametrisations, see figs. C.1 to C.4. In addition, both panels compare our results with the experimental frequency shift. We find a discrepancy of 26% to 35% between the experiment and theoretical frequency shifts. Similarly, fig. 3.3 shows the standard King's plot combining both pairing schemes. In this case, the relative error amounts to 2%, which is two times larger than in fig. 3.2 (when we treated each pairing scheme independently), because fig. 3.3 incorporates the pairing uncertainty. In the previous sections we discussed that, typically, the pairing uncertainty has a noticeable impact on the propagated uncertainties of the nuclear quantities of interest for isotopic shift calculations, see tables 3.4 and 3.5. However, there are some cases in which the pairing uncertainty is smaller than the code's precision, e.g. in fig. 3.3 the first blue point starting from the left, has smaller uncertainties in comparison to the other points. The

Figure 3.2.: Standard King Plot, see eq. (1.22), for $\alpha : {}^2S_{1/2} \rightarrow {}^2D_{5/2}$, and $\beta : {}^2S_{1/2} \rightarrow {}^2D_{3/2}$ transitions for pairs of neighbouring even-even Yb^+. Theoretical results in blue are obtained isotopes using the SLY4 parametrisation and BCS (Left) and LN (Right) pairing schemes, with errorbars calculated with eq. (3.13). The red lines indicate the best linear fit to the four points and the black points indicate experimental values [5].

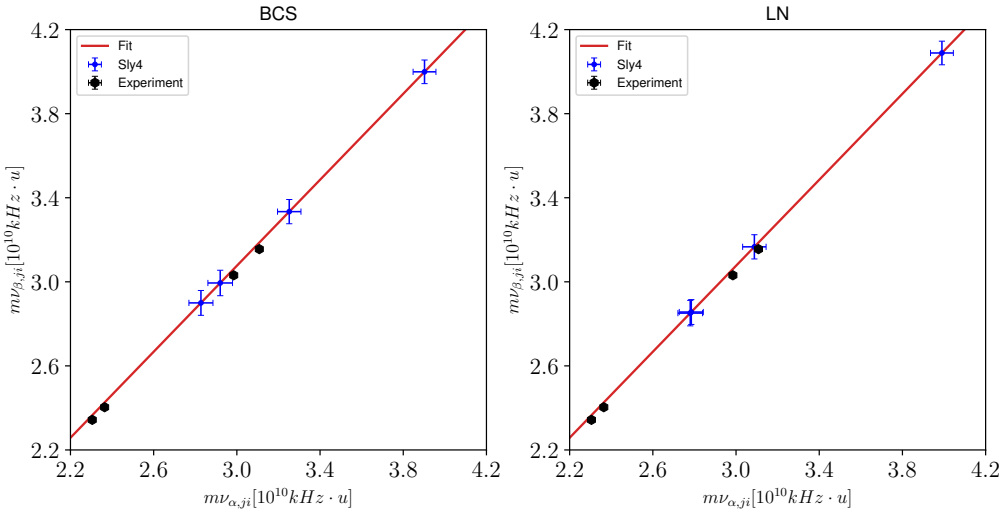

Figure 3.3.: Same caption details as fig. 3.2 but including both the BCS and LN pairing schemes.

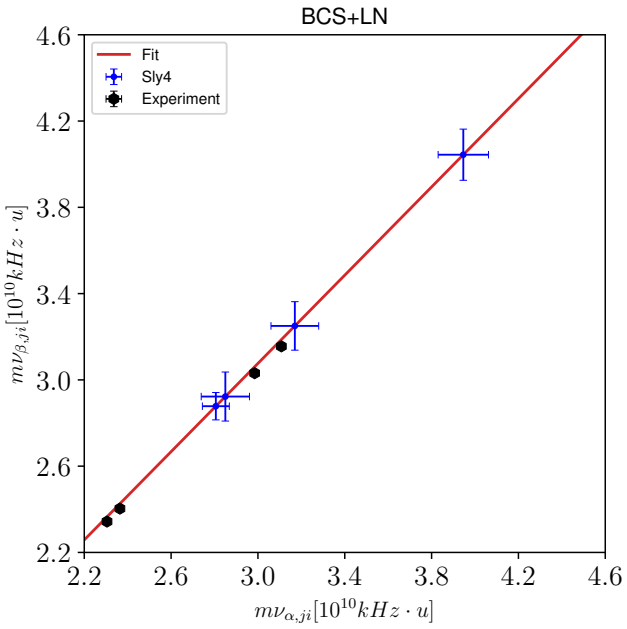

Table 3.8.: Frequency shift of the α transition with its uncertainty. Both quantities are extracted from the experiment taken from Ref.[5].

Isotope pair (j, i)	$\nu_{\alpha,ji}$ $[kHz]$
(168, 170)	2 179 098.93(21)
(170, 172)	2 044 854.78(34)
(172, 174)	1 583 068.42(36)
(174, 176)	1 509 055.29(28)

discrepancy between the experiment and the theoretical frequency shift does not improve when we include the pairing uncertainty.

Eventually, with the current method used within this section we reproduce King's linear relation between both modified frequency shifts. However, theoretical uncertainties on $m\nu_{\alpha,ji}$ and $m\nu_{\beta,ji}$ it could only describe non-linearities larger than 1%-2%. Therefore, with the current approach nuclear theory uncertainties prevent the identification of an experimental non-linearity as a sign of physics beyond the SM. In the following section we introduce an alternative approach in order to avoid these large theoretical uncertainties introduced by the FS term.

3.6. Another approach: Non-linearity based on a experimentally measured frequency shift

Here we present an alternative way to predict the deviations from linearity of the Yb^+ isotopic chain. The main idea is to reduce the uncertainties getting rid of the main source of theoretical error in our calculations, that is, the FS term, with an error dominated by the theoretical uncertainty in $\delta\langle r^2\rangle_{ji}$, see eq. (1.22). For this purpose, we use the experimentally measured frequency shift of the α transition, with its uncertainty, in order to calculate the frequency shift of the β transition. In this way we take advantage of the fact that the relative error of the experimental data is about $1 \cdot 10^{-7}$ to $2 \cdot 10^{-7}$, see table 3.8. This error is way smaller than the theoretical relative error obtained in section 3.5, about 1% to 2%.

Therefore, in this new approach we only have to determine $m\nu_{\beta,ji}$ from the $m\nu_{\alpha,ji}$ transition. In virtue of eq. (1.22)

$$m\nu_{\beta,ji} = K_{\beta\alpha} + F_{\beta\alpha} m\nu_{\alpha,ji} + G^{(2)}_{\beta\alpha} m \left[\delta\langle r^2\rangle_{ji}\right]^2 + G^{(4)}_{\beta\alpha} m\delta\langle r^4\rangle_{ji},$$

where the definitions of the atomic quantities $K_{\beta\alpha}$, $F_{\beta\alpha}$, $G^{(2)}_{\beta\alpha}$ and $G^{(4)}_{\beta\alpha}$ are below the eqs. (1.16)

and (1.19). The theoretical frequency shift uncertainty $\varepsilon_{m\nu_{\beta,ji}}$ is given by

$$\varepsilon_{m\nu_{\beta,ji}} = \sqrt{\left(\frac{\partial m\nu_{\beta,ji}}{\partial m\nu_{\alpha,ji}}\varepsilon_{\nu_{m\alpha,ji}}\right)^2 + \left(\frac{\partial m\nu_{\beta,ji}}{\partial(m\delta\langle r^2\rangle_{ji})}\varepsilon_{m\delta\langle r^2\rangle_{ji}}\right)^2 + \left(\frac{\partial \nu_{m\beta,ji}}{\partial(m\delta\langle r^4\rangle_{ji})}\varepsilon_{m\delta\langle r^4\rangle_{ji}}\right)^2}$$

$$= \sqrt{\left(F_{\beta\alpha}\varepsilon_{m\nu_{\alpha,ji}}\right)^2 + \left(2G^{(2)}_{\beta\alpha}m\delta\langle r^2\rangle_{ji}\varepsilon_{m\delta\langle r^2\rangle_{ji}}\right)^2 + \left(G^{(4)}_{\beta\alpha}\varepsilon_{m\delta\langle r^4\rangle_{ji}}\right)^2}. \tag{3.15}$$

In contrast to eq. (3.13), eq. (3.15) has two main advantages. On the one hand, the theoretical differential squared charge radius error coming from the FS term has been replaced by the measured frequency shift of the α transition. This replacement does not impact the prediction of theoretical deviations from linearity as the FS is linear by definition and, consequently, does not contribute to the non-linearity. On the other hand, the redefinition of the atomic parameters also leads to smaller uncertainties in the NL terms as $G^{(2)}_{\beta\alpha}$ is suppressed by a factor of $\simeq 44$ with respect to $G^{(2)}_{\alpha}$, and $G^{(2)}_{\beta}$ and $G^{(4)}_{\beta\alpha}$ is suppressed by a factor of $\simeq 2000$ with respect to $G^{(4)}_{\beta}$ and $G^{(4)}_{\alpha}$, see table 3.6.

Figures 3.4 and 3.5 show the King's Plot obtained using the SLY4 Skyrme parametrisation with BCS and LN pairing schemes, respectively. They take into account the experimental values and errors for each $m\nu_{\alpha,ji}$ point and compute $m\nu_{\beta}$ and its uncertainty in virtue of eqs. (1.22) and (3.15), respectively. The red line indicates a linear fit to the former points. A deviation from linearity is observed when we zoom our points by a factor of 10^6 in both figures. In contrast to section 3.5, the theoretical uncertainties are typically smaller than the deviation from linearity, except for the $(168, 170)$ point with the BCS pairing scheme and $(174, 176)$ with the LN pairing scheme, where deviation from linearity are of the same order as the theoretical uncertainties . For $(168, 170)$, the horizontal and vertical errorbars are larger than in other isotope pairs due to a larger experimental uncertainty in the inverse-mass difference, see table 3.7. Comparing figs. 3.4 and 3.5 the same deviation pattern is observed. From $(174, 176)$ to $(168, 170)$: (- + - +), where "+" indicates that the point deviates upwards with respect to the red line (linearity) and "-" indicates that the point deviates downwards.

The results obtained with other Skyrme parametrisations can be found in appendix D. For different Skyrme parametrisation there is a pattern discrepancy, see figs. D.1 to D.7. In particular, SKI3 shows a (+ - - +) deviation pattern with the VDI pairing interaction and with the DDDI pairing interaction and LN pairing scheme, see figs. D.1 and D.4b, respectively. Meanwhile, for UNEDF0, UNEDF1 and SkI3 with DDDI pairing interaction and BCS pairing scheme the deviation from linearity is of the order of the theoretical uncertainty and, consequently, it is unclear whether the calculated points are linear or not, see figs. D.4a, D.5 and D.7

Figure 3.4.: Same King's plot as fig. 3.2 but based on the experimental $\nu_{\alpha,ji}$ value and its error, extracted from [5]. The vertical errorbars include the theoretical uncertainties in the modified frequency shift $m\nu_{\beta,ji}$, see eq. (3.15). The insets zoom the points by a factor of 10^6.

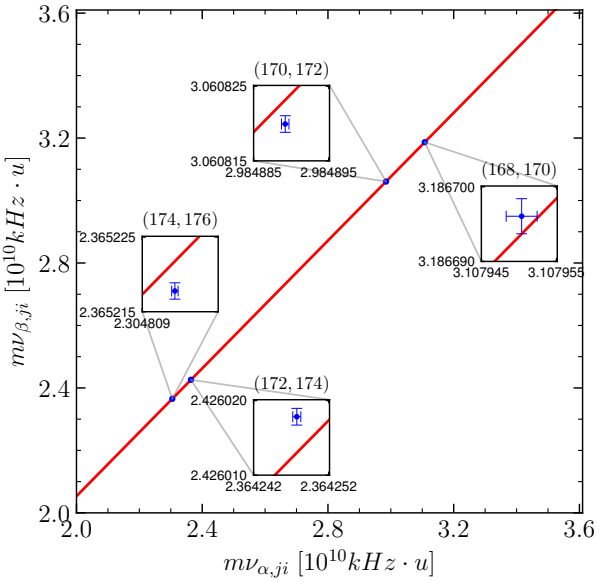

Figure 3.5.: Same details as fig. 3.4 but using the LN pairing scheme.

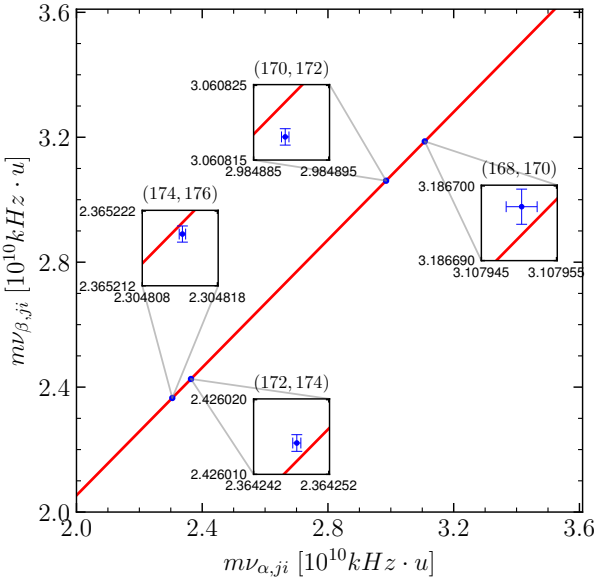

Figure 3.6 is the same plot as in figs. 3.4 and 3.5 the combination of both pairing schemes for the SLY4 parametrisation. In this scenario, the introduction of the paring uncertainty increases the total theoretical uncertainty in $m\nu_{\beta,ji}$, in general, hampering the theoretical prediction of non-linearities. Nonetheless, two out of the four points, $(170, 172)$ and $(172, 174)$ evidence a non linear behaviour when we include the pairing uncertainty into the total uncertainty in our calculations. A similar behaviour appears for the remaining parametrisations. In particular, see figs. D.10a to D.12b appendix D show large theoretical uncertainties in $m\nu_{\beta,ji}$ hamper the possibility to assign a theoretical deviation from linearity from our nuclear calculations.

In the literature, there is disagreement on which is the dominant NL term in eq. (1.22). For instance, in Ref.[5] it is pointed out that the QFS is the dominant NL term, while in Ref.[8] stated that the FOMS is the largest source of non-linearity. In order to study the impact of each NL term in our calculations, we present the following approach. First we define two modified frequency shifts that shall only take into account one out of the two NL terms, that is

$$m\nu^{(QFS)}_{\beta,ji} = K_{\beta\alpha} + F_{\beta\alpha} m\nu_{\alpha,ji} + G^{(2)}_{\beta\alpha}[m\delta\langle r^2\rangle_{ji}]^2, \tag{3.16}$$

for the QFS term. Its associated theoretical uncertainty is written as follows

Figure 3.6.: Same caption details as in fig. 3.4 but using both pairing schemes.

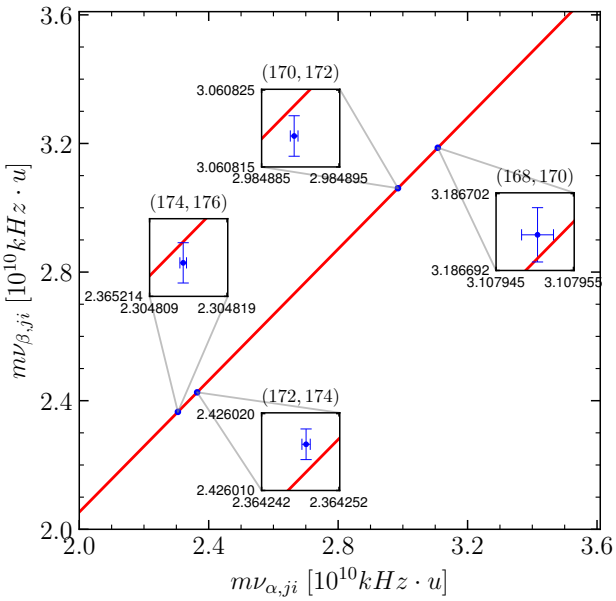

$$\varepsilon_{\nu^{(QFS)}_{\beta,ji}} = \sqrt{\left(\frac{\partial \nu^{(QFS)}_{\beta,ji}}{\partial \mu_{ji}}\varepsilon_{\mu_{ji}}\right)^2 + \left(\frac{\partial \nu^{(QFS)}_{\beta,ji}}{\partial\left(\delta\langle r^2\rangle_{ji}\right)}\varepsilon_{\delta\langle r^2\rangle_{ji}}\right)^2 + \left(\frac{\partial \nu^{(QFS)}_{\beta,ji}}{\partial \nu_{\alpha,ji}}\varepsilon_{\nu_{\alpha,ji}}\right)^2} =$$

$$= \sqrt{\left(K_{\beta\alpha}\varepsilon_{\mu_{ji}}\right)^2 + \left(F_{\beta\alpha}\varepsilon_{\nu_{\alpha,ji}}\right)^2 + \left(2G^{(2)}_{\beta\alpha}\delta\langle r^2\rangle_{ji}\varepsilon_{\delta\langle r^2\rangle_{ji}}\right)^2}, \tag{3.17}$$

Likewise, we do the same for the FOMS term,

$$m\nu^{(FOMS)}_{\beta,ji} = K_{\beta\alpha} + F_{\beta\alpha}m\nu_{\alpha,ji} + G^{(4)}_{\beta\alpha}m\delta\langle r^4\rangle_{ji}, \tag{3.18}$$

with theoretical uncertainty given by

$$\varepsilon_{\nu^{(FOMS)}_{\beta,ji}} = \sqrt{\left(\frac{\partial \nu^{(FOMS)}_{\beta,ji}}{\partial \mu_{ji}}\varepsilon_{\mu_{ji}}\right)^2 + \left(\frac{\partial \nu^{(FOMS)}_{\beta,ji}}{\partial\left(\delta\langle r^4\rangle_{ji}\right)}\varepsilon_{\delta\langle r^4\rangle_{ji}}\right)^2 + \left(\frac{\partial \nu^{(FOMS)}_{\beta,ji}}{\partial \nu_{\alpha,ji}}\varepsilon_{\nu_{\alpha,ji}}\right)^2} =$$

$$= \sqrt{\left(K_{\beta\alpha}\varepsilon_{\mu_{ji}}\right)^2 + \left(F_{\beta\alpha}\varepsilon_{\nu_{\alpha,ji}}\right)^2 + \left(G^{(4)}_{\beta\alpha}\varepsilon_{\delta\langle r^4\rangle_{ji}}\right)^2}. \tag{3.19}$$

Furthermore, we adopt the approach followed in [5] to quantify the deviation from

Figure 3.7.: Residual deviations from linearity in the King's plot using the SLY4 parametrisation and the BCS pairing scheme. Theoretical deviations caused by both FOMS and QFS terms are shown as blue circles, while those caused by the QFS term are shown as magenta squares and for the FOMS term as green triangles. The points are shifted from the central $m\nu_{\alpha,ji}$ value for clarity.

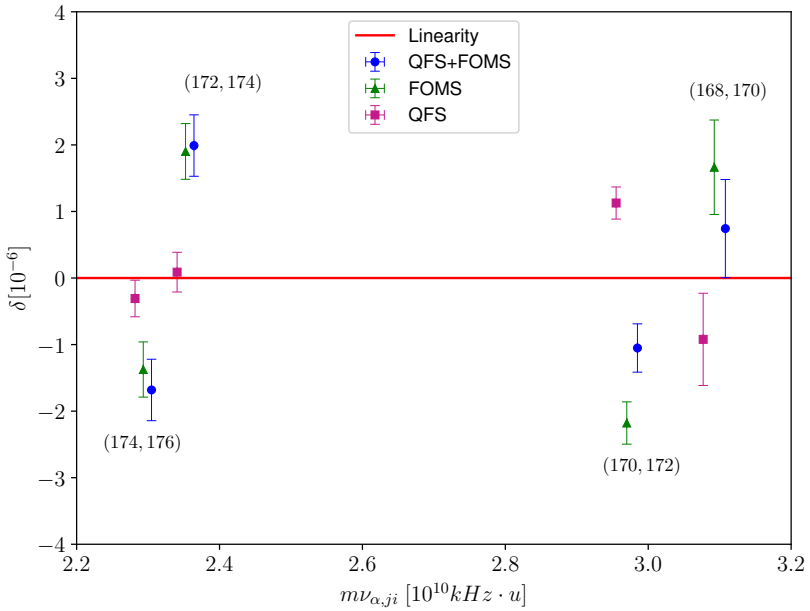

linearity. In order to do so, we make a linear fit for each set of points $\{m\nu_{\alpha,ji}, m\nu_{\beta,ji}\}$, $\{m\nu_{\alpha,ji}, m\nu_{\beta,ji}^{(QFS)}\}$ and $\{m\nu_{\alpha,ji}, m\nu_{\beta,ji}^{(FOMS)}\}$. Thus, the resulting fitted points, namely $m\nu_{\beta,ji}^{(fit)}$, $m\nu_{\beta,ji}^{(QFS)(fit)}$ and $m\nu_{\beta,ji}^{(FOMS)(fit)}$ describe a linear relation with $m\nu_{\alpha}$. The resulting residual deviation from linearity is obtained as follows

$$\delta = \frac{m\nu_{\beta,ji} - m\nu_{\beta,ji}^{(fit)}}{m\nu_{\beta,ji}}. \tag{3.20}$$

Neither Ref.[5] nor Ref.[8] give an estimation of the uncertainties associated to δ with their calculations and assumptions. In this work we propose the following approach in order to quantify the theoretical deviation uncertainty. First we take the minimum and maximum vertical deviations of a given point $\{m\nu_{\alpha,ji}, m\nu_{\beta,ji}\}$ with respect to the linear fit $m\nu_{\beta,ji}$, that is

$$\delta^{(min)} \equiv \frac{min\left(m\nu_{\beta,ji} \pm \varepsilon\nu_{\beta,ji} - m\nu_{\beta,ji}^{(fit)}\right)}{m\nu_{\beta,ji}}, \tag{3.21}$$

$$\delta^{(max)} \equiv \frac{max\left(m\nu_{\beta,ji} \pm \varepsilon\nu_{\beta,ji} - m\nu_{\beta,ji}^{(fit)}\right)}{m\nu_{\beta,ji}} \tag{3.22}$$

Figure 3.8.: Same caption details as fig. 3.7 but using the LN pairing scheme.

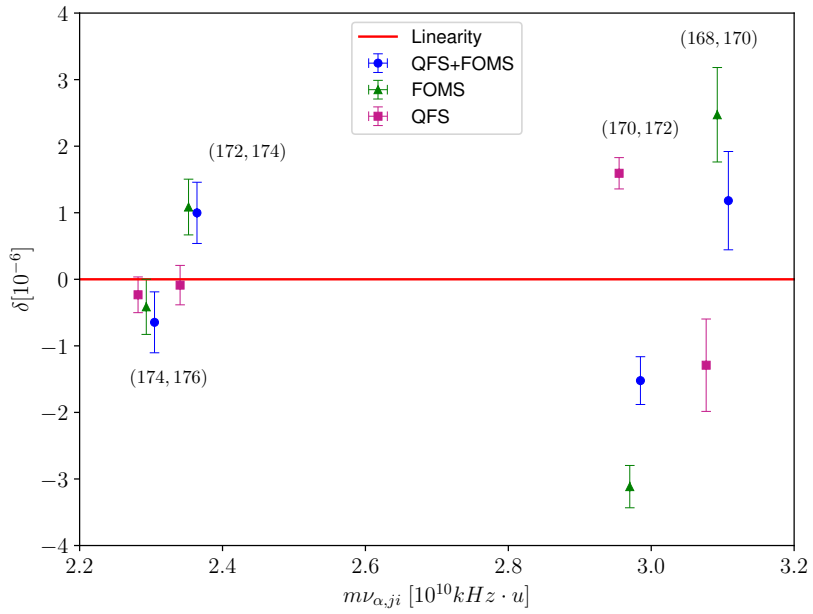

Figure 3.9.: Same as fig. 3.7 but for the combined BCS and LN pairing schemes.

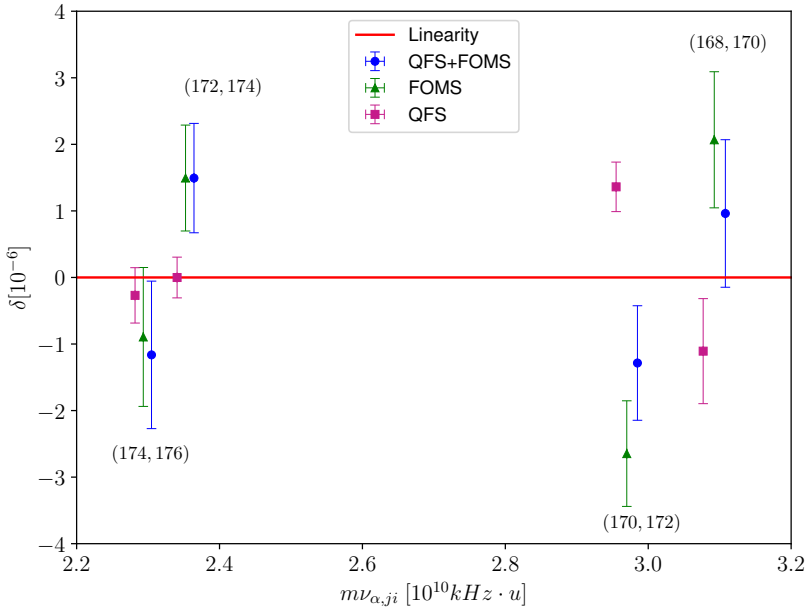

Then, the theoretical deviation uncertainty is given by

$$\varepsilon_\delta = \frac{\delta^{(max)} - \delta^{(min)}}{2}. \tag{3.23}$$

Figures 3.7 and 3.8 show the contribution of the QFS and the FOMS NL terms to the total deviation from linearity, labelled in the figures as QFS+FOMS, using SLY4 with BCS and LN pairing schemes, respectively. The red line represents the King's linear relation. In fig. 3.7 the total non-linearity (QFS+FOMS) is found in between the QFS (magenta) and FOMS (green) deviations for two isotope pairs, $(168, 170)$ and $(170, 172)$, because the FOMS and QFS deviations are opposite in sign. Consequently, the total deviation has the sign of the dominant NL term which in this case is the FOMS term. To contrast, for $(172, 174)$ and $(174, 176)$ isotope pairs both FOMS and QFS NL contributions are share the same sign, here the dominant term is again the FOMS term. In appendix E, see figs. E.9 to E.12, we show the deviation from linearity for the remaining Skyrme parametrisations. They systematically predict a predominance of the FOMS term as the main source of non-linearity within the SM, in agreement with Ref.[8].

Figure 3.9 shows the residual deviation taking into account the combination of BCS and LN pairing schemes. Here the error in the y-axis is larger than in each pairing scheme independently because of the pairing uncertainty. In some pairs like $(168, 170)$

Figure 3.10.: Residual deviations from the linearity of the King's plot with all four parametrisations used in this work and BCS+LN pairing schemes compared to experiment [5]. The points have been displaced in the horizontal axis for visibility.

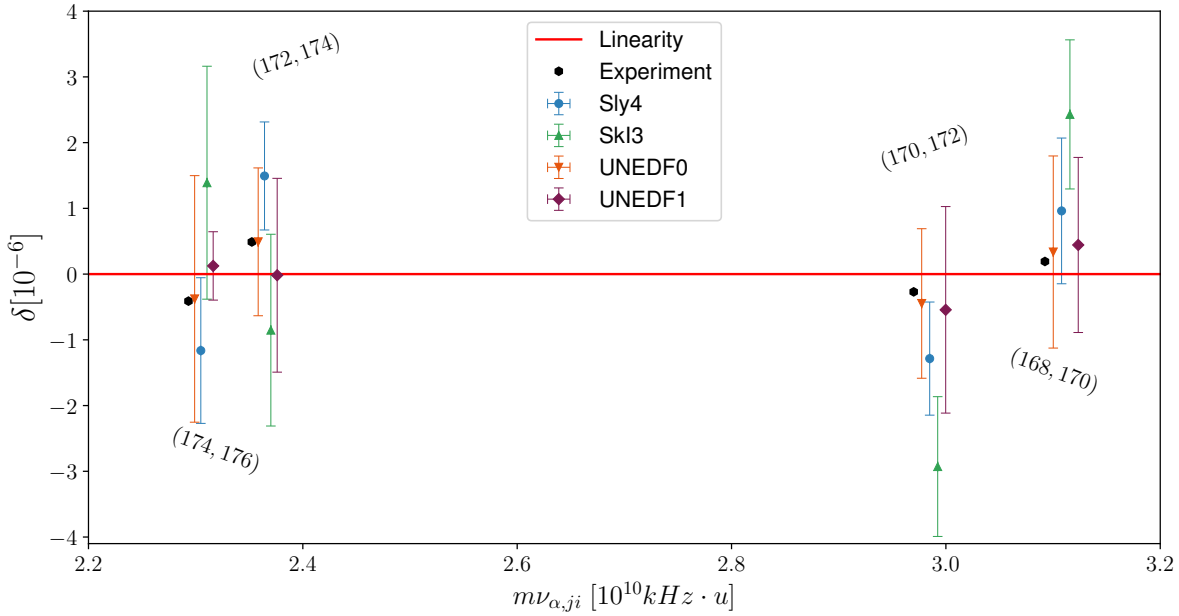

and (174, 176) the uncertainty associated to the theoretical deviations is larger than the theoretical deviation. We find deviations from linearity for the remaining isotopes. Nonetheless, including theoretical uncertainties the leading source of non-linearity is the FOMS term. The corresponding figures for the other Skyrme forces are collected in appendix E, see figs. E.9 to E.12. For SkI3 we also find deviations from linearity for some isotope pairs, see figs. E.9 and E.10, dominated by the FOMS term. However, for UNEDF0 and UNEDF1 the theoretical uncertainty is larger than the deviation from linearity for all isotope pairs, which hinders any possible discussion of non-linearity.

Figures 3.10 and 3.11 summarise the main results of this work. In both figures we exclude SkI3 with VDI pairing interaction for simplicity. Figure 3.11 gathers the theoretical deviations for each isotope pair for all four Skyrme parametrisations combining BCS and LN pairing schemes. On the one hand, for SLy4 and SkI3 we find that, for some isotopes pairs, the theoretical deviation from linearity is larger than its theoretical uncertainty. For these Skyrme forces we conclude that our calculations predict a NL behaviour of the order $\delta \sim 10^{-6}$. On the other hand, UNEDF0 and UNEDF1 predict 10^{-7} deviations from linearity which seems rather promising since this is the order of

Figure 3.11.: Same caption details as fig. 3.10 but using LN pairing scheme.

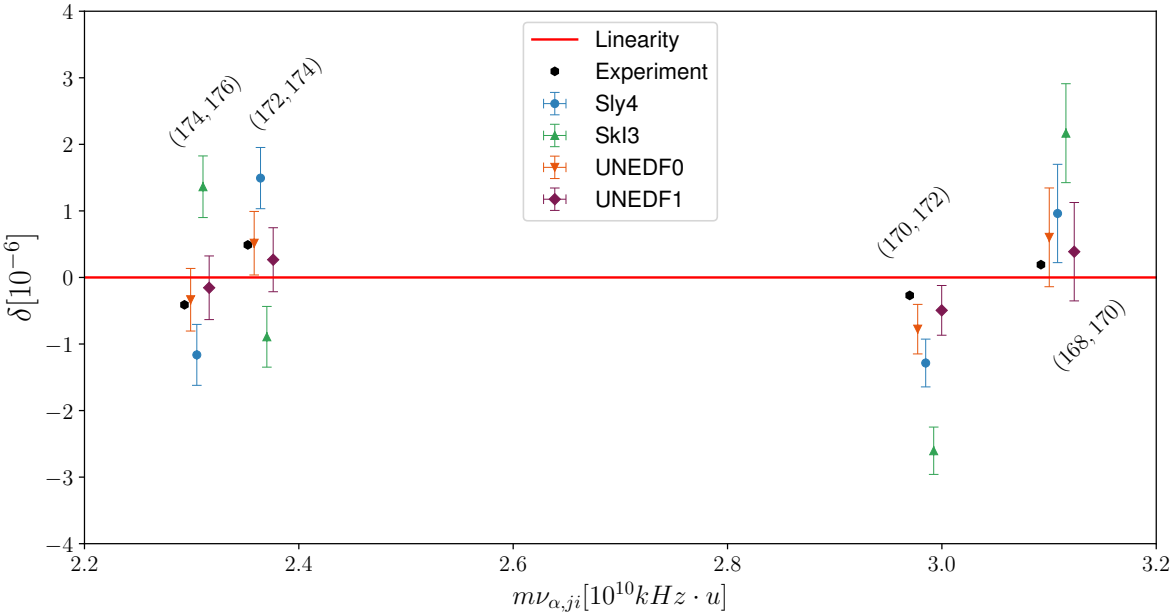

magnitude found in experiment [5]. However, the theoretical uncertainties for these parametrisations are $\varepsilon_\delta \sim 5 \cdot 10^{-7}$, which are significantly larger than the theoretical deviations. Therefore, the current level of uncertainty for these Skyrme forces prevents any prediction of non-linearities. The main source of uncertainty in fig. 3.10 is due to the propagation error of the pairing uncertainty.

To overcome the theoretical limitation introduced by the pairing uncertainty, we represent the same plot but now considering only the LN pairing scheme. The main motivation of this plot is to consider only one pairing scheme and test if the uncertainty of the IS non-linearity is smaller than its magnitude in a systematic manner. The predilection in choosing the LN pairing scheme is arbitrary since the results with BCS pairing scheme are similar. In this figure the uncertainty drops significantly, allowing the prediction of deviations from linearity for UNEDF0 and UNEDF1. This result is very encouraging because allows us to identify two Skyrme parametrisations with $\delta \sim 10^{-7}$ NL behaviour in the Yb IS, in agreement with the experiment [5].

3.6.1. Discrepancy with respect to Counts et.al

In this subsection we expand on the discrepancy between our results and these of [5]. Our results predict larger contributions of the FOMS term for all Skyrme forces used within this work. On the contrary, Ref.[5] assumed a proportional relation between $\langle r^4\rangle_i$ and $\langle r^2\rangle_i$, expected to hold over different isotopes:

$$\langle r^4\rangle_i = b\Big[\langle r^2\rangle_i\Big]^2. \tag{3.24}$$

Under this assumption, eq. (1.18) is rewritten as follows,

$$m\nu_{\alpha,ji} = K_\alpha + F_\alpha m\delta\langle r^2\rangle_{ji} + G_\alpha m\Big[\delta\langle r^2\rangle_{ji}\Big]^2, \tag{3.25}$$

where $G_\alpha \equiv G_\alpha^{(2)} + bG_\alpha^{(4)}$ is the effective QFS electronic factor.

Ref.[5] concludes that the main source of non-linearity within the SM is the QFS. In table 3.9, we present the b ratio using both $\langle r^4\rangle$ and $\langle r^2\rangle$ obtained with SLY4 parametrisation. The values of b for the remaining parametrisations can be found in Appendix F.

Table 3.9.: $\langle r^4\rangle$-to-$\langle r^2\rangle$ ratio, b ,see eq. (3.24), for Yb isotopes with the SLY4 Skyrme parametrisation. $\Delta b/\overline{b}$ stands for the fractional variation, where Δb is the standard deviation of b coefficients divided by their mean value, $\overline{b}$.

Yb isotope	BCS		LN	
	b	$\Delta b/\overline{b}$	b	$\Delta b/\overline{b}$
168	1.2517		1.2518	
170	1.2519		1.2522	
172	1.2510	0.0016	1.2512	0.0018
174	1.2500		1.2495	
176	1.2469		1.2468	

$$\delta\nu_{\beta\alpha}^{NL} = G_{\beta\alpha}^{(2)}\Big[\delta\langle r^2\rangle_{ji}\Big]^2 + G_{\beta\alpha}^{(4)}\delta\langle r^4\rangle_{ji} \tag{3.26}$$

$$= G_{\beta\alpha}\Big[\delta\langle r^2\rangle_{ji}\Big]^2, \tag{3.27}$$

where $G_{\beta\alpha} = G_{\beta\alpha}^{(2)} + bG_{\beta\alpha}^{(4)}$. Again, eq. (3.26) holds generally but eq. (3.27) is true if and only if b relation holds. Table 3.9 we show the b-ratio of the Yb isotopic chain of interest within this work. In appendix F we show the b ratio with the remaining parametrisations, see tables F.1 to F.4. In our calculations we find a 0.1% deviation in b for consecutive

isotopes. This dependence of b on the transition suggests that the assumption in [5] may not hold for Yb, and explains why in our calculations we found the FOMS to be the dominant NL term in contrast to the experiment [5].

4. Summary and conclusions

In this work we have calculated the deviations, within the SM, from King's linear relation between the IS of four neighbouring pairs of even-even Yb isotopes with zero nuclear spin on two narrow optical quadrupole transitions $^2S_{1/2} \rightarrow {}^2D_{3/2}$, $^2S_{1/2} \rightarrow {}^2D_{5/2}$.

For this purpose, we used a state-of-the-art many-body nuclear code, SkyAx, that enabled us to solve the HF equations for five ^{A}Yb isotopes, $A \in \{168, 170, 172, 174, 176\}$ in two spatial dimensions assuming axial symmetry using Skyrme forces as interaction model and the inclusion of pairing interaction at the BCS level. The use of SkyAx in this work was justified mainly by two features of the code. First, the current implementation of SkyAx is restricted to even-even nuclei with axial deformation. Second, the HFB+BCS model is valid for well-bound nuclei far from the neutron and proton drip lines where a full Hartree-Fock-Bogoliugov treatment would be more suitable. SkyAx provided several Skyrme functionals –Sly4, SkI3, UNEDF0, UNEDF1 have been selected in this work– with a density-dependent pairing functional handled at the BCS level, optionally with an approximate particle-number projection Lipkin-Nogami scheme.

We have associated a theoretical uncertainty to the point-proton radii, R_p and R_{p4}, by varying the grid spacing, d_r and d_z, and the grid dimension, L_r and L_z, on a particular Yb isotope. The uncertainty introduced by the code's precision is $1.4\dot{1}0^{-4}$fm. In addition, we have introduced another source of uncertainty due to the discrepancies between the point-proton radii between the BCS and LN pairing schemes given a particular Skyrme force. We have found that, typically, the pairing uncertainty has a noticeable impact on the total theoretical uncertainty for both point-proton radii and varied between different isotopes. For a few isotopes, the pairing uncertainty was smaller than the code's precision. If this case happened for the same isotope (or isotopes) for different Skyrme forces, this could be a direct evidence of nuclear structure effects for these isotopes. However, this seems to happen arbitrarily for the isotopic Yb chain when using different Skyrme forces.

We have calculated the relevant nuclear quantities for IS measurements in addition to their uncertainties from the error propagation of the uncertainties in the point-proton radii. At this point, we have taken the approximation of neglecting spin-orbit contributions on the calculation of the charge radii, $\langle r^2 \rangle$ and $\langle r^4 \rangle$. However, for $\langle r^2 \rangle$ we would

like to stress that recent publications on this subject predict corrections up to $0.01 fm$ and, since $\delta\langle r^2\rangle$ is sensible to variations of the rms charge radius, these corrections should be taken into account in the future. More precisely, the Yb isotopes considered in this work are open-shell systems in which contributions from deformed spin-orbit densities could be appreciable. At least, these corrections should be larger than the code's precision ,$1.4 \cdot 10^{-4} fm$, in order to have a noticeable impact in the results presented in this work. In addition, we took $\langle r^4\rangle \simeq (R_{p4})^4$ as a first approximation, assuming that the corrective terms would not have any impact on $\delta\langle r^4\rangle$. In this sense, our results should not have been affected by the corrective terms in $\langle r^4\rangle$ if the magnitude of these corrections were smaller than the theoretical uncertainty in R_{p4}. Nonetheless, the impact of the corrective terms in $\delta\langle r^4\rangle$ are of the order of $0.3 fm^4$ for the $(170, 172)$ isotope pair, which is of the same order of the uncertainty in R_{p4} when we computed the two pairing schemes. A more detailed study in this direction is an aspect of our work that should be improved in the future.

Combining the nuclear quantities determined in this work and the atomic parameters given by Refs.[5, 8] we have determined the theoretical frequency shifts, $m\nu_{\alpha,ji}$ and $m\nu_{\beta,ji}$. Nonetheless, the theoretical uncertainty introduced by the FS term overshadowed any possible discrimination of deviation from linearity within the SM. In order to solve that, we have adopted another approach that had two main advantages with respect the previous approach. First, a strong suppression in the atomic parameters. Second, experimentally measured frequency shifts for the α transition with a relative error of $2 \cdot 10^{-7}$, at most. Both assets led to a noticeable reduction of $m\nu_{\beta,ji}$ uncertainty, allowing us to determine some features about the evidence for non-linear IS in Yb^+.

We have observed a discrepancy between the non-linear deviation patterns when we used different Skyrme forces. In particular, for SLY4 we have found that the observed deviation pattern is (+ - + -) whereas for SKI3 the deviation pattern is (+ - - +), for some pairing schemes. However, for UNEDF0 and UNEDF1 the observed deviations from linearity were typically smaller than the theoretical uncertainty in δ. This obstructed any deviation pattern prediction for these parametrisations.

We have also calculated the contributions of each NL term within the SM to the total deviation from the linearity. To do that, we have computed the deviations from linearity following the same procedure as Ref.[5]. We have fitted the predicted IS to its best linear regression. The deviation δ from linearity was then computed taking the relative difference between each point from its linear fit. In addition we have proposed and determined the theoretical uncertainties in δ, which has never been done in previous works on this topic. All Skyrme forces systematically predicted a predominance of the FOMS term over the QFS term as a main source of non-linearity within the SM. These results are

in agreement with Ref.[8] and in disagreement with Ref.[5]. In Ref.[5] they assumed a correlation, $\langle r^4 \rangle = b \langle r^2 \rangle^2$, where b was expected to be identical for all Yb isotopes. We computed the b ratio for all Skyrme forces and found a 0.1% deviation between different isotopes. This dependence of b suggests that the main assumption in Ref.[5] may not hold for Yb. This could explain the discrepancy between our results and the experiment [5] on which is the dominant NL term within the SM.

Eventually, we have been able to predict deviations from linearity for all four Skyrme forces. For SLY4 and SKI3 we have been able to predict deviations from linearity even considering the pairing uncertainty. The deviations from linearity with these Skyrme forces are $\delta \sim 10^{-6}$ which are one order of magnitude larger than the experiment [5]. UNEDF0 and UNEDF1 did not predict any deviation from linearity when we include the pairing uncertainty, due to the fact the uncertainty was greater than the current deviation from linearity. However, the predicted deviations by UNEDF0 and UNEDF1 are of $\delta \sim 10^{-7}$. This seems quite encouraging since this is the order of magnitude predicted by the experiment [5]. In order to overcome the limitation on the prediction of non-linearities when we included the pairing scheme, we have considered the results with each pairing scheme. In this case, the only source of theoretical uncertainty was due to the code's precision. This consideration reduced the deviation uncertainty, allowing us to predict deviations from linearity of the same order of magnitude as the experiment [5] for UNEDF0 and UNEDF1.

A. Appendix A

In this appendix we derive the formal definition of the field isotope shift employed in eq. (1.9) following the steps detailed in [13]. This procedure does have an impact on the resulting King Plot and non-linearities studied in this work since it is derived taking into account some considerations and approximations and, consequently, it is of utter importance show its derivation. The following procedure is principally based on a central-field approximation which provides the foundation of the theory. The objective is thus to find the energy difference from one isotope to another, of a single electron in an s state outside closed shells. In virtue of first-order perturbation theory we can split the field shift as a product of two quantities [13]: in one hand a transition-dependent, isotope-independent parameter, N, and on the other hand, a transition-independent, isotope-dependent parameter, namely Λ. The frequency shift associated is therefore written as follows:

$$\nu = \frac{\delta E}{h} = \frac{1}{h} N\Lambda, \tag{A.1}$$

where h is the Planck constant. The first term in eq. (A.1), N is the relativistic probability density of the electron being at the origin, $r = 0$. This term is insensitive to the form of the nuclear charge distribution and it is depends on the electronic structure of the particular atomic state . The second term in eq. (A.1), Λ, depends on the nuclear charge distribution of both isotopes, thus a nuclear-dependent parameter, and is written as follows

$$\Lambda = N\Big(\frac{Ze^2}{4\pi\epsilon_0}\Big)\lambda, \tag{A.2}$$

where λ is the so-called Seltzer moment [12] and it is defined as follows:

$$\lambda = \sum_{n=2}^{\infty} S_n \delta\langle r^n\rangle_{ji}, \tag{A.3}$$

where $\langle r^n\rangle = \frac{\int \rho(r) r^n r^2 dr}{\int \rho(r) r^2 dr}$ and $S_n = \frac{6}{n(n+1)}$ are the coefficients of the changes in $\langle r^n\rangle$. Therefore, the Seltzer moment expansion relates the field shift and the expansion of the radial electron density which contains the functional dependence of the radial probability

density on r (supplemental material in [5]). One can rearrange some terms in eq. (A.1) and obtain:

$$\nu^{FS}_{\alpha,ji} = \sum_{n=2}^{\infty} \frac{c\alpha' Z}{2\pi} \frac{\xi^{(n)}_{\alpha}}{n(n+1))} \delta\langle r^n \rangle_{ji} = \sum_{n=2}^{\infty} H^{(n)}_{\alpha} \delta\langle r^n \rangle_{ji} \tag{A.4}$$

where $\alpha' \simeq 1/137$ is the fine-structure constant. It can be shown that the first four odd coefficients of the Seltzer moment expansion, are typically zero [13]. Therefore, expanding eq. (A.4) up to the second non-zero term one obtains:

$$\nu^{FS}_{\alpha,ji} = H^{(2)}_{\alpha} \delta\langle r^2 \rangle_{ji} + H^{(4)}_{\alpha} \delta\langle r^4 \rangle_{ji} + \mathcal{O}(\delta\langle r^6 \rangle_{ji}), \tag{A.5}$$

in our notation $H^{(2)}_{\alpha} \equiv F_{\alpha}$ and $H^{(4)}_{\alpha} \equiv G^{(4)}_{\alpha}$. The first term in eq. (A.5) is the leading term of this expansion, that is the reason why is often called the field shift -even though it is not- and the second term is called fourth moment shift throughout this work and it is regarded as a source of non-linearity in King's Plot.

B. Appendix B

In this appendix we list the nuclear properties calculated with the nuclear many-body SkyAx code and the remaining Skyrme parametrisations discussed in chapter 3.

B.1. Point-Proton radius

Here are listed the theoretical values of the point-proton radius obtained with the remaining Skyrme parametrisations. All calculations take into account their respective theoretical uncertainty discussed and computed in sections 3.1.1 and 3.1.2. In tables B.1 to B.3 we show the predicted point-proton radius using SkI3, UNEDF0 and UNEDF1 Skyrme parametrisations, respectively.

Table B.1.: Point-proton radius of neighbouring even-even Yb isotopes extracted from SkyAx using SkI3 skyrme parametrisation.

	$R_p\ [fm]$					
Isotope	VDI			DDDI		
	BCS	LN	BCS+LN	BCS	LN	BCS+LN
^{168}Yb	5.20722(14)	5.20811(14)	5.20766(47)	5.20778(14)	5.20830(14)	5.20804(30)
^{170}Yb	5.22638(14)	5.22459(14)	5.22549(90)	5.22603(14)	5.22598(14)	5.22600(14)
^{172}Yb	5.23923(14)	5.23934(14)	5.23928(15)	5.23877(14)	5.23932(14)	5.23905(31)
^{174}Yb	5.25082(14)	5.25150(14)	5.25116(37)	5.25017(14)	5.25065(14)	5.25041(28)
^{176}Yb	5.26312(14)	5.26320(14)	5.26316(15)	5.26233(14)	5.26296(14)	5.26264(34)

Table B.2.: Same caption details as table B.1 but using UNEDF0 parametrisation.

Isotope	$R_p\ [fm]$		
	BCS	LN	BCS+LN
^{168}Yb	5.21863(14)	5.21961(14)	5.21912(51)
^{170}Yb	5.23618(14)	5.23730(14)	5.23674(58)
^{172}Yb	5.25236(14)	5.25215(14)	5.25225(17)
^{174}Yb	5.26663(14)	5.26577(14)	5.26620(45)
^{176}Yb	5.27948(14)	5.27831(14)	5.27890(60)

Table B.3.: Same caption details as table B.1 but using UNEDF1 parametrisation.

Isotope	$R_p\ [fm]$		
	BCS	LN	BCS+LN
^{168}Yb	5.22943(14)	5.22945(14)	5.22944(14)
^{170}Yb	5.24701(14)	5.24628(14)	5.24665(39)
^{172}Yb	5.26211(14)	5.26123(14)	5.26167(46)
^{174}Yb	5.27516(14)	5.27513(14)	5.27515(14)
^{176}Yb	5.28828(14)	5.28841(14)	5.28835(16)

B.2. Fourth moment point-proton radius

Here are listed the theoretical values of the fourth order point-proton radius obtained with the remaining Skyrme parametrisations. All calculations take into account their respective theoretical uncertainty discussed and computed in sections 3.1.1 and 3.1.2. In tables B.4 to B.6 we show the predicted fourth order point-proton radius using SKI3, UNEDF0 and UNEDF1 Skyrme parametrisations, respectively.

Table B.4.: Fourth moment point-proton radius of neighbouring even-even Yb isotopes extracted from SKYAX code using SKI3 Skyrme parametrisation.

Isotope	$R_p^{(4)}\ [fm]$					
	VDI			DDDI		
	BCS	LN	BCS+LN	BCS	LN	BCS+LN
^{168}Yb	5.55563(14)	5.55669(14)	5.55616(54)	5.55621(14)	5.55678(14)	5.55650(32)
^{170}Yb	5.57719(14)	5.57441(14)	5.5758(14)	5.57610(14)	5.57591(14)	5.57601(17)
^{172}Yb	5.58816(14)	5.58831(14)	5.58823(16)	5.58718(14)	5.58800(14)	5.58759(43)
^{174}Yb	5.59742(14)	5.59838(14)	5.59790(50)	5.59623(14)	5.59687(14)	5.59655(35)
^{176}Yb	5.60793(14)	5.60805(14)	5.60799(15)	5.60661(14)	5.60749(14)	5.60705(46)

Table B.5.: Same caption details as table B.4 but using UNEDF0 parametrisation.

Isotope	$R_p^{(4)}\ [fm]$		
	BCS	LN	BCS+LN
^{168}Yb	5.56959(14)	5.57036(14)	5.56997(41)
^{170}Yb	5.58775(14)	5.58908(14)	5.58841(68)
^{172}Yb	5.60399(14)	5.60378(14)	5.60388(18)
^{174}Yb	5.61765(14)	5.61669(14)	5.61717(50)
^{176}Yb	5.62950(14)	5.62809(14)	5.62877(74)

Table B.6.: Same caption details as table B.4 but using UNEDF1 parametrisation.

Isotope	$R_p^{(4)}$ $[fm]$		
	BCS	LN	BCS+LN
^{168}Yb	5.57654(14)	5.57583(14)	5.57618(38)
^{170}Yb	5.59444(14)	5.59295(14)	5.59369(76)
^{172}Yb	5.60882(14)	5.60733(14)	5.60808(76)
^{174}Yb	5.62021(14)	5.62009(14)	5.62015(15)
^{176}Yb	5.63168(14)	5.63185(14)	5.63177(16)

B.3. Charge radius

Here are listed the predicted theoretical values for the charge radius obtained with the remaining Skyrme parametrisations. All calculations take into account their respective theoretical uncertainty discussed and computed in section 3.2. In tables B.7 to B.9 we show the predicted charge radius using SkI3, UNEDF0 and UNEDF1 Skyrme parametrisations, respectively.

Table B.7.: Charge radius of neighbouring even-even Yb isotopes using SkI3 skyrme parametrisation.

Isotope	$\langle r^2 \rangle^{1/2}$ $[fm]$					
	VDI			DDDI		
	BCS	LN	BCS+LN	BCS	LN	BCS+LN
^{168}Yb	5.25925(33)	5.26013(33)	5.25969(55)	5.25980(33)	5.26032(33)	5.26006(42)
^{170}Yb	5.27791(34)	5.27614(34)	5.27702(94)	5.27756(34)	5.27750(34)	5.27753(33)
^{172}Yb	5.29031(34)	5.29042(34)	5.29037(34)	5.28986(34)	5.29041(34)	5.29013(43)
^{174}Yb	5.30149(35)	5.30216(35)	5.30182(48)	5.30084(35)	5.30131(34)	5.30108(41)
^{176}Yb	5.31335(35)	5.31343(35)	5.31339(35)	5.31257(35)	5.31319(35)	5.31288(47)

Table B.8.: Same caption details as table B.7 but using UNEDF0 parametrisation.

Isotope	$\langle r^2 \rangle^{1/2}$ $[fm]$		
	BCS	LN	BCS+LN
^{168}Yb	5.27055(33)	5.27152(33)	5.27103(58)
^{170}Yb	5.28761(34)	5.28872(34)	5.28816(65)
^{172}Yb	5.30332(34)	5.30311(34)	5.30322(35)
^{174}Yb	5.31714(34)	5.31629(34)	5.31672(55)
^{176}Yb	5.32956(35)	5.32840(35)	5.32898(68)

Table B.9.: Same caption details as table B.7 but using UNEDF1 parametrisation.

Isotope	$\langle r^2 \rangle^{1/2}$ $[fm]$		
	BCS	LN	BCS+LN
^{168}Yb	5.28124(33)	5.28126(33)	5.28125(33)
^{170}Yb	5.29834(34)	5.29761(33)	5.29798(49)
^{172}Yb	5.31298(34)	5.31210(34)	5.31254(55)
^{174}Yb	5.32559(34)	5.32556(34)	5.32558(34)
^{176}Yb	5.33828(35)	5.33841(35)	5.33834(35)

B.4. Differential squared charge radius

Here are listed the predicted theoretical values for the differential squared charge radius obtained with the remaining Skyrme parametrisations. All calculations take into account their respective theoretical uncertainty discussed and computed in section 3.3. In tables B.10 to B.12 we show the predicted differential squared charge radius using SKI3, UNEDF0 and UNEDF1 Skyrme parametrisations, respectively.

Table B.10.: Differential squared charge radius of consecutive even-even Yb isotope pairs using SKI3 Skyrme parametrisation.

Yb isotope pair (j,i)	$\delta\langle r^2\rangle_{ji}\ [fm^2]$					
	VDI			DDDI		
	BCS	LN	BCS+LN	BCS	LN	BCS+LN
(168, 170)	-0.1966(21)	-0.1871(21)	-0.1919(40)	-0.1688(21)	-0.1811(21)	-0.1749(76)
(170, 172)	-0.1311(21)	-0.1301(21)	-0.1306(37)	-0.1510(21)	-0.1362(21)	-0.1436(75)
(172, 174)	-0.1184(21)	-0.1162(21)	-0.1173(47)	-0.1243(21)	-0.1155(21)	-0.1199(49)
(174, 176)	-0.1259(21)	-0.1245(21)	-0.1252(58)	-0.1197(21)	-0.1260(21)	-0.1229(51)

Table B.11.: Same caption details as table B.10 but using UNEDF0 parametrisation.

Yb isotope pair (j,i)	$\delta\langle r^2\rangle_{ji}\ [fm^2]$		
	BCS	LN	BCS+LN
(168, 170)	-0.1801(21)	-0.1816(21)	-0.1809(80)
(170, 172)	-0.1664(21)	-0.1525(21)	-0.1594(63)
(172, 174)	-0.1468(21)	-0.1399(21)	-0.1434(51)
(174, 176)	-0.1322(21)	-0.1288(21)	-0.1306(80)

Table B.12.: Same caption details as table B.10 but using UNEDF1 parametrisation.

Yb isotope pair	$\delta\langle r^2\rangle_{ji}$ $[fm^2]$		
(j,i)	BCS	LN	BCS+LN
(168, 170)	-0.1809(21)	-0.1730(21)	-0.1770(44)
(170, 172)	-0.1553(21)	-0.1537(21)	-0.1545(64)
(172, 174)	-0.1342(21)	-0.1432(21)	-0.1387(51)
(174, 176)	-0.1353(21)	-0.1369(21)	-0.1361(22)

B.5. Differential fourth moment charge radius

Here are listed the predicted theoretical values for the differential fourth moment charge radius obtained with the remaining Skyrme parametrisations. All calculations take into account their respective theoretical uncertainty discussed and computed in section 3.4. In tables B.13 to B.15 we show the predicted differential fourth moment charge radius using SKI3, UNEDF0 and UNEDF1 Skyrme parametrisations, respectively.

Table B.13.: Differential fourth Seltzer moment charge radius of consecutive even-even Yb isotope pairs using SKI3 Skyrme parametrisation.

Yb isotope pair (j,i)	$\delta\langle r^4\rangle_{ji}\ [fm^4]$					
	VDI			DDDI		
	BCS	LN	BCS+LN	BCS	LN	BCS+LN
(168, 170)	-14.87(14)	-13.72(14)	-14.29(44)	-12.22(14)	-13.20(14)	-12.71(54)
(170, 172)	-7.63(14)	-7.70(14)	-7.66(53)	-9.67(14)	-8.41(14)	-9.04(55)
(172, 174)	-6.48(14)	-6.33(21)	-6.40(56)	-7.05(14)	-6.21(14)	-6.62(56)
(174, 176)	-7.38(14)	-7.29(14)	-7.34(64)	-6.80(14)	-7.46(14)	-7.13(58)

Table B.14.: Same caption details as table B.13 but using UNEDF0 parametrisation.

Yb isotope pair (j,i)	$\delta\langle r^4\rangle_{ji}\ [fm^4]$		
	BCS	LN	BCS+LN
(168, 170)	-12.61(14)	-13.01(14)	-12.81(55)
(170, 172)	-11.38(14)	-10.30(14)	-10.84(49)
(172, 174)	-9.65(14)	-9.12(21)	-9.38(38)
(174, 176)	-8.43(14)	-8.07(14)	-8.25(64)

Table B.15.: Same caption details as table B.10 but using UNEDF1 parametrisation.

Yb isotope pair	$\delta\langle r^4\rangle_{ji}$ $[fm^4]$		
(j,i)	BCS	LN	BCS+LN
(168, 170)	-12.48(14)	-11.92(14)	-12.20(59)
(170, 172)	-10.11(14)	-10.11(14)	-10.11(75)
(172, 174)	-8.06(14)	-9.03(21)	-8.54(54)
(174, 176)	-8.17(14)	-8.38(14)	-8.28(16)

C. Appendix C

In this appendix we show the same plots as in section 3.5 with the remaining Skyrme parametrisations. In figs. C.1 to C.4 we have considered both paring schemes independently and propagated the corresponding theoretical uncertainty. In contrast, in figs. C.6a to C.8b we have included the pairing uncertainty into the total theoretical uncertainty in order to check the impact in the resulting King's plot.

Figure C.1.: Standard King Plot, see eq. (1.22), for $\alpha : {}^2S_{1/2} \rightarrow {}^2D_{5/2}$, and $\beta : {}^2S_{1/2} \rightarrow {}^2D_{3/2}$ transitions for pairs of neighbouring even-even Yb^+. Theoretical results in blue are obtained isotopes using the SKI3 Skyrme parametrisation with VDI pairing interaction and BCS (Left) and LN (Right) pairing schemes, with errorbars calculated with eq. (3.13). The red lines indicate the best linear fit to the four points and the black points indicate experimental values [5].

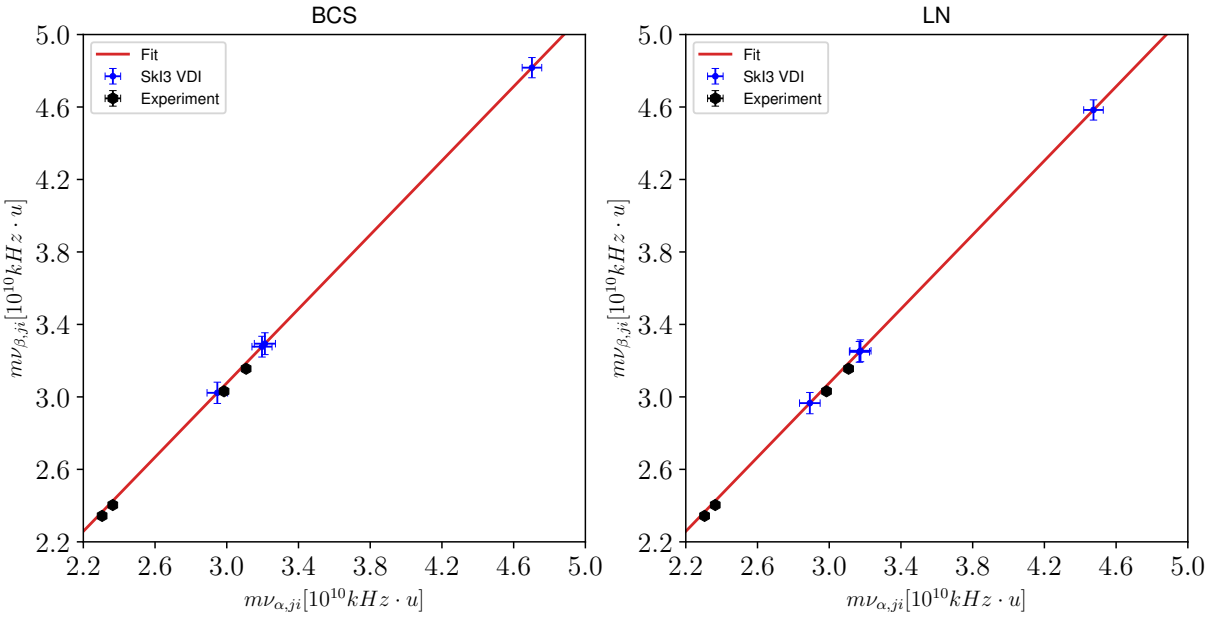

Figure C.2.: Same caption details as fig. C.1 but using DDDI pairing interaction.

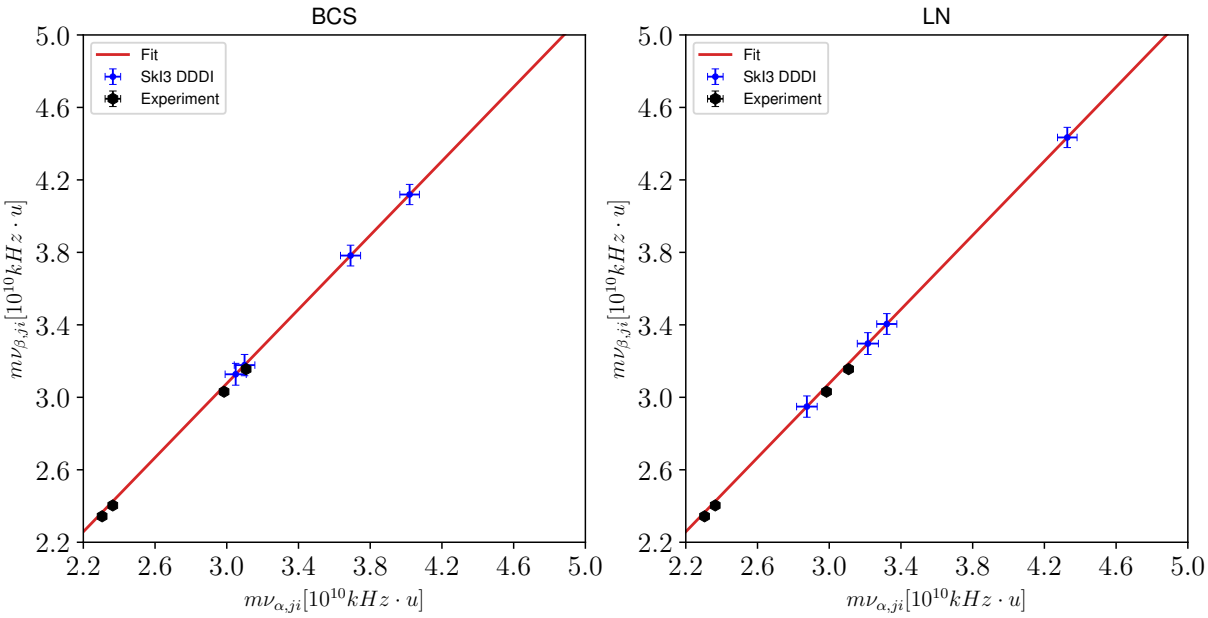

Figure C.3.: Same caption details as fig. C.1 but using the UNEDF0 parametrisation.

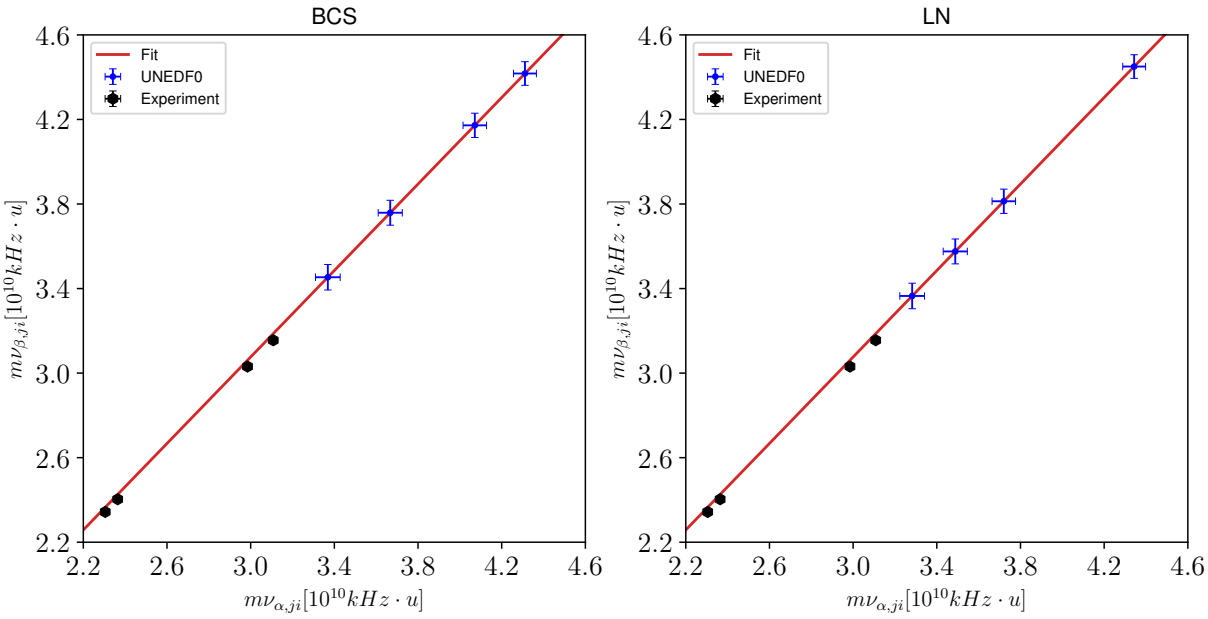

Figure C.4.: Same caption details as fig. C.1 but using the UNEDF1 parametrisation.

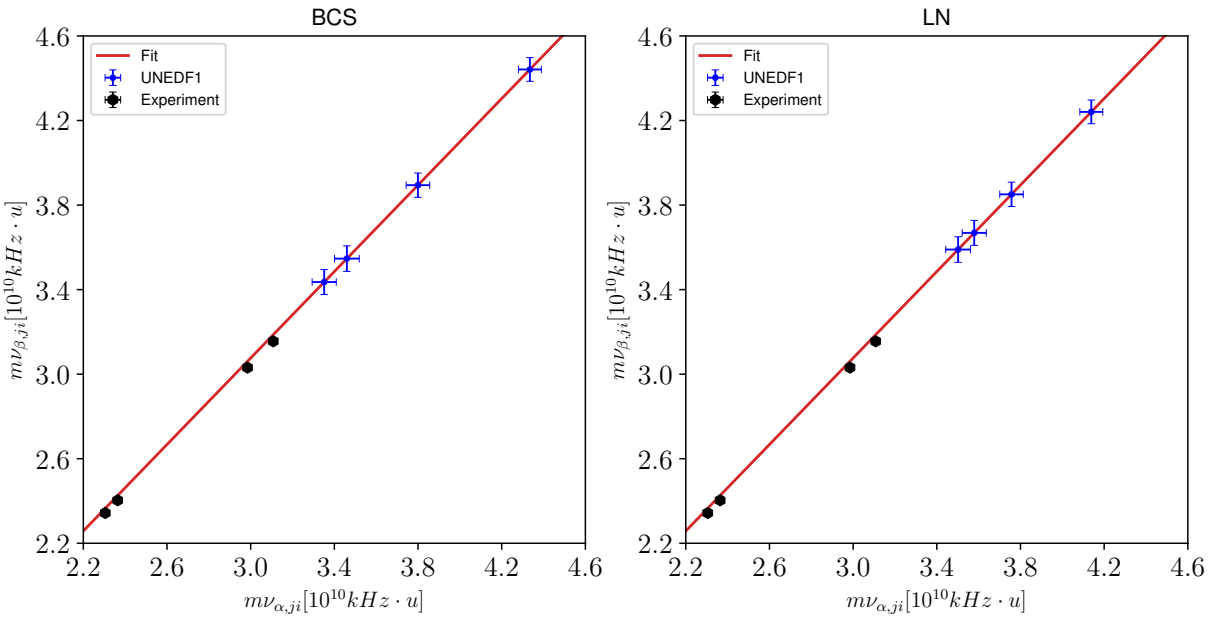

Figure C.5.: Same caption details as fig. C.1 but using using a combination of the two pairing schemes (BCS+LN). Left panel: with VDI pairing interaction. Right panel: with DDDI pairing interaction.

(a) SkI3 VDI

(b) SkI3 DDDI

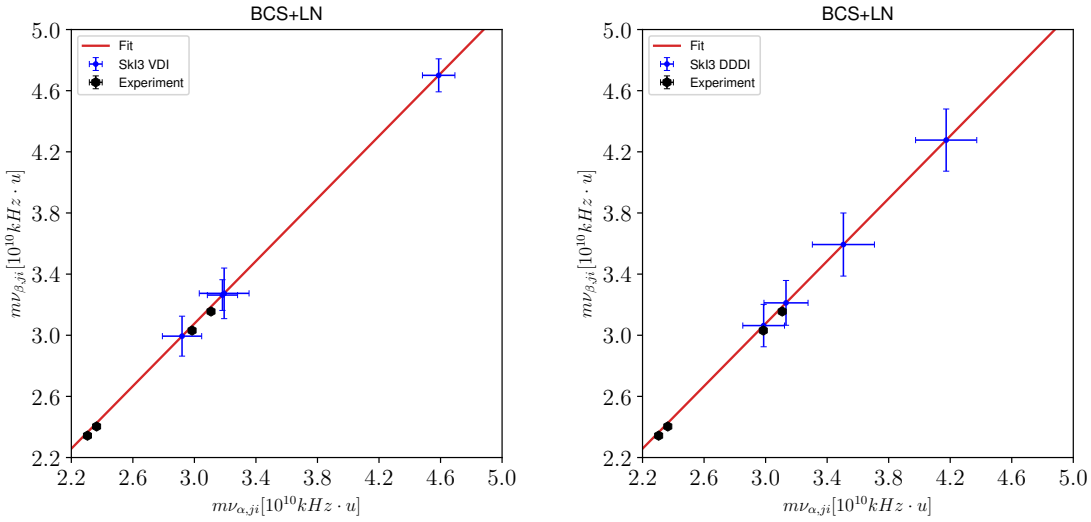

Figure C.7.: Same caption details as fig. C.1 but using using a combination of the two pairing schemes (BCS+LN). Left panel: UNEDF0 Skyrme parametrisation. Right panel:UNEDF1 Skyrme parametrisation.

(a) UNEDF0

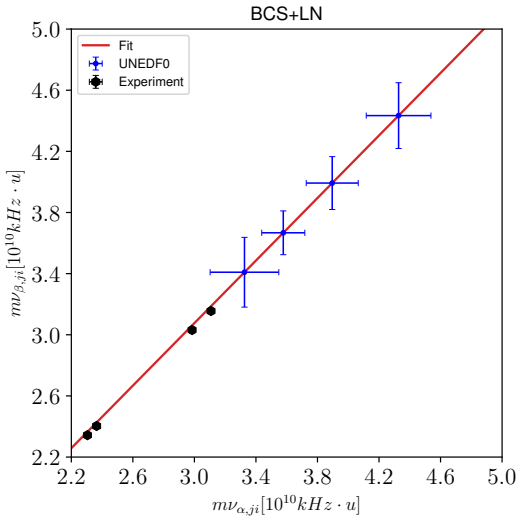

(b) UNEDF1

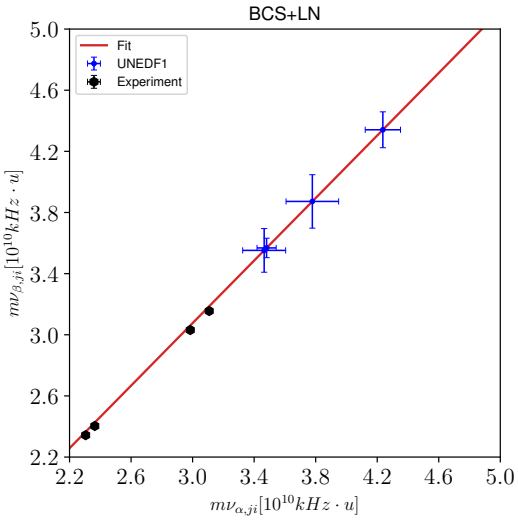

D. Appendix D

In this appendix we show the King's plot with the remaining Skyrme parametrisations using the new approach presented in section 3.6. In figs. D.2a to D.8b we have considered both paring schemes independently and propagated the corresponding theoretical uncertainty. In contrast, in figs. D.10a to D.12b we have included the pairing uncertainty into the total theoretical uncertainty in order to check the impact in the resulting King's plot.

Figure D.1.: King's plot based on the experimental $\nu_{\alpha,ji}$ value and its error, extracted from [5] with SKI3 with VDI pairing interaction and: (a) BCS pairing scheme, (b) LN pairing shceme. The vertical errorbars include the theoretical uncertainties in the modified frequency shift $m\nu_{\beta,ji}$, see eq. (3.15). The insets zoom the points by a factor of 10^6.

(a) BCS

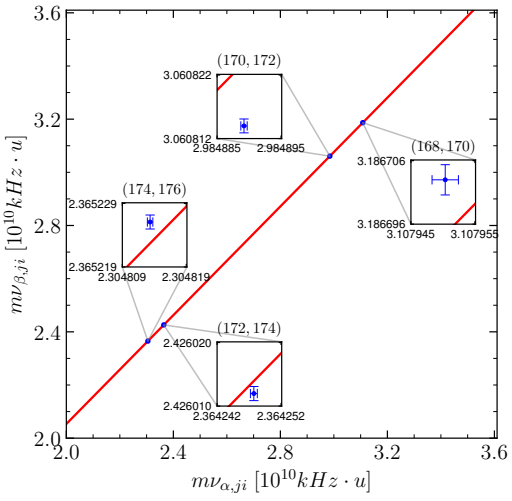

(b) LN

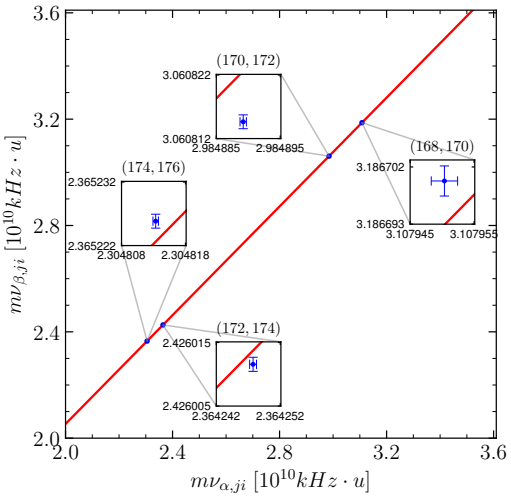

Figure D.3.: Same caption as in fig. D.1 but with DDDI pairing interaction.

(a) BCS

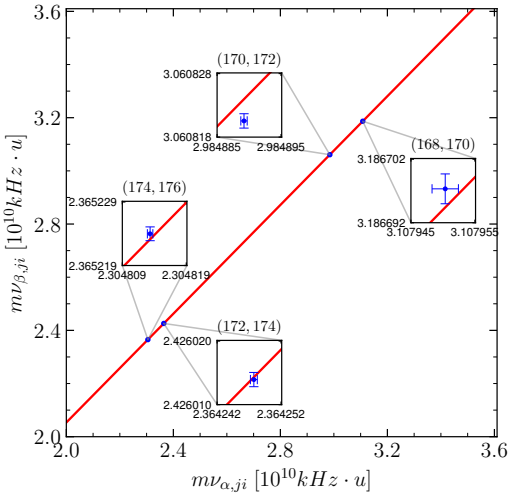

(b) LN

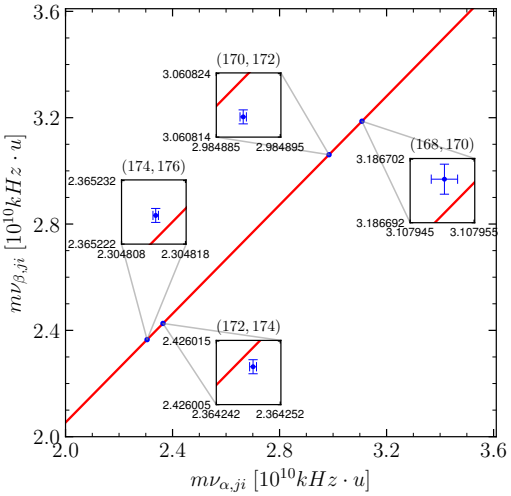

Figure D.5.: Same caption as in fig. D.1 but with UNEDF0 pairing interaction.

(a) BCS

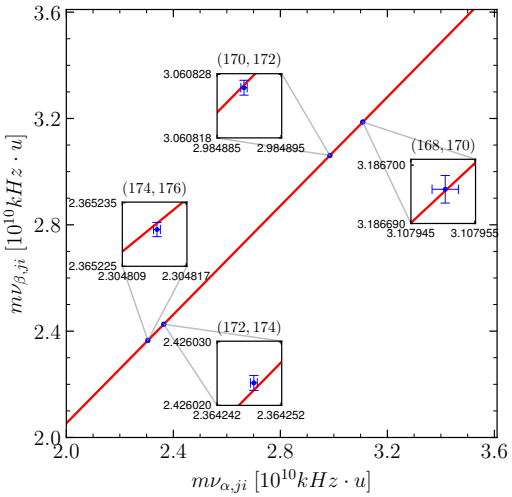

(b) LN

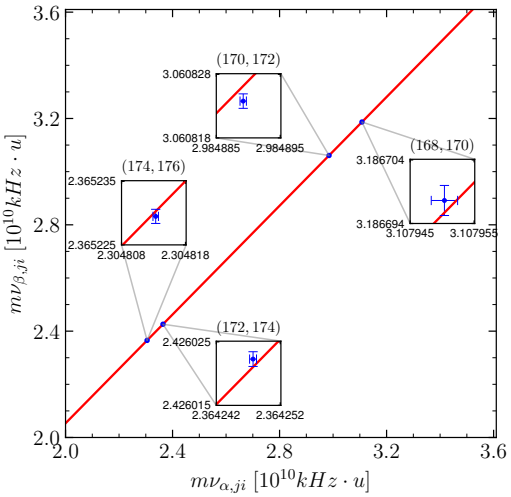

Figure D.7.: Same caption as in fig. D.1 but with UNEDF0 pairing interaction.

(a) BCS (b) LN

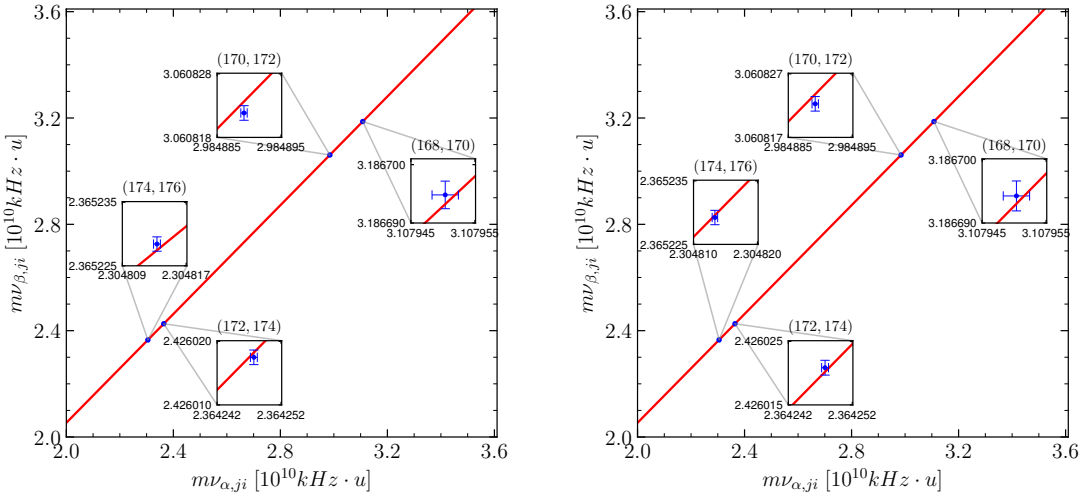

Figure D.9.: Same caption as in fig. D.1 but using a combination of the two pairing schemes (BCS+LN) for: (a) VDI pairing interaction. (b) DDDI pairing interaction.

(a) SkI3 VDI (b) SkI3 DDDI

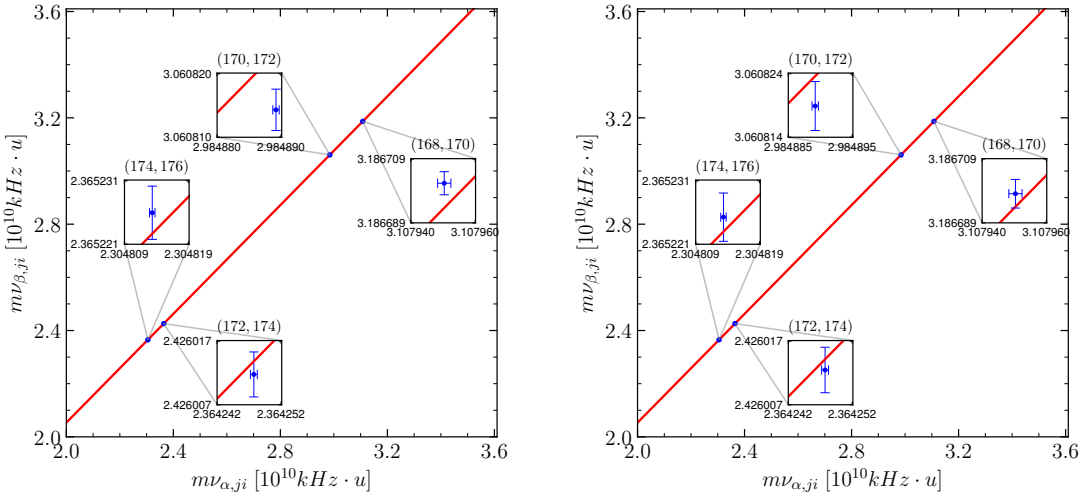

Figure D.11.: Same caption as in fig. D.1 but using a combination of the two pairing schemes (BCS+LN) for: (a) UNEDF0. (b) UNEDF1.

(a) UNEDF0

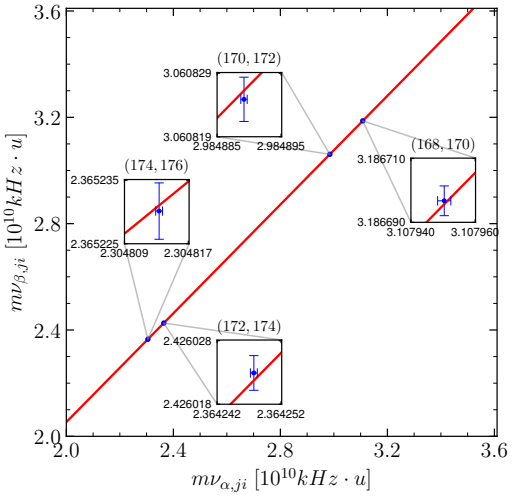

(b) UNEDF1

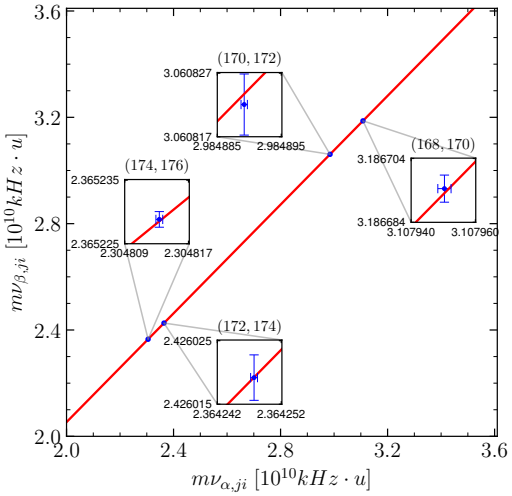

E. Appendix E

In this appendix we show the predicted theoretical deviation from linearity and its NL contributions presented in section 3.6 for the remaining Skyrme parametrisations. In figs. E.1 to E.8 we have considered both paring schemes independently and propagated the corresponding theoretical uncertainty. In contrast, in figs. E.9 to E.12 we have included the pairing uncertainty into the total theoretical uncertainty in order to check the impact in the resulting King's plot.

Figure E.1.: Residual deviations from linearity in the King's plot using the SKI3 parametrisation with VDI pairing interaction and the BCS pairing scheme. Theoretical deviations caused by both FOMS and QFS terms are shown as blue circles, while those caused by the QFS term are shown as magenta squares and for the FOMS term as green triangles. The points are shifted from the central $m\nu_{\alpha,ji}$ value for clarity.

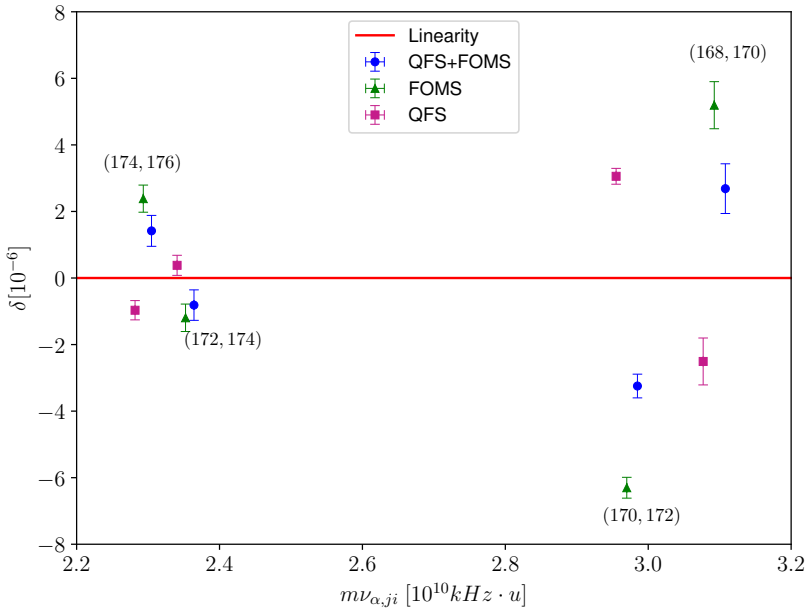

Figure E.2.: Same caption details as fig. E.1 but with the LN pairing scheme.

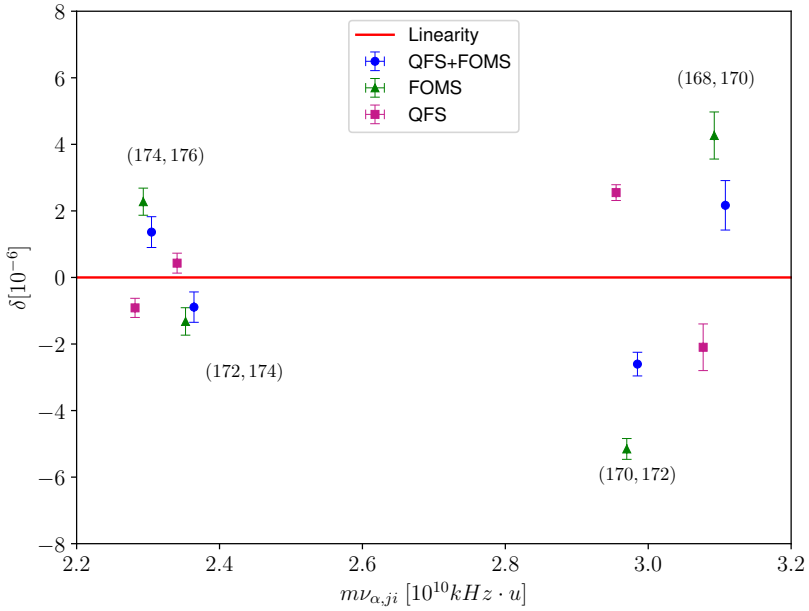

Figure E.3.: Same caption details as fig. E.1 but with DDDI pairing interaction and BCS pairing scheme.

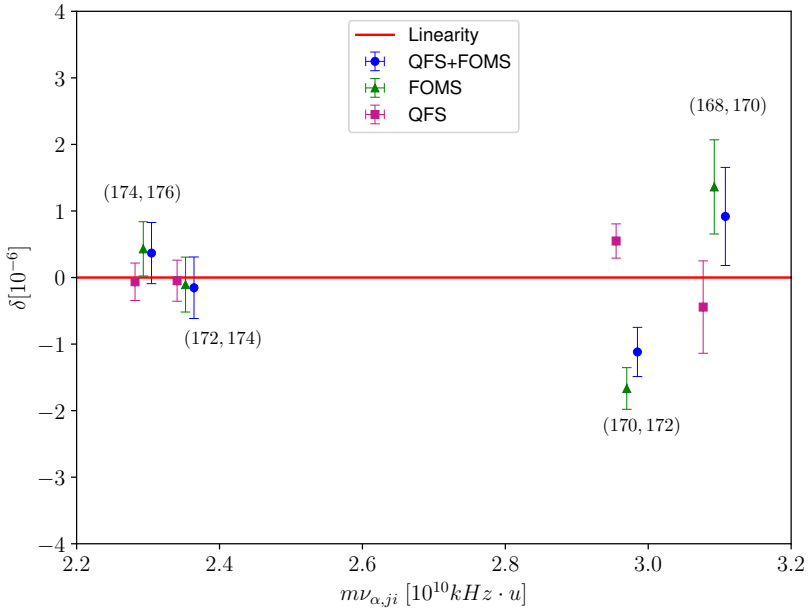

Figure E.4.: Same caption details as fig. E.1 but with DDDI pairing interaction and LN pairing scheme.

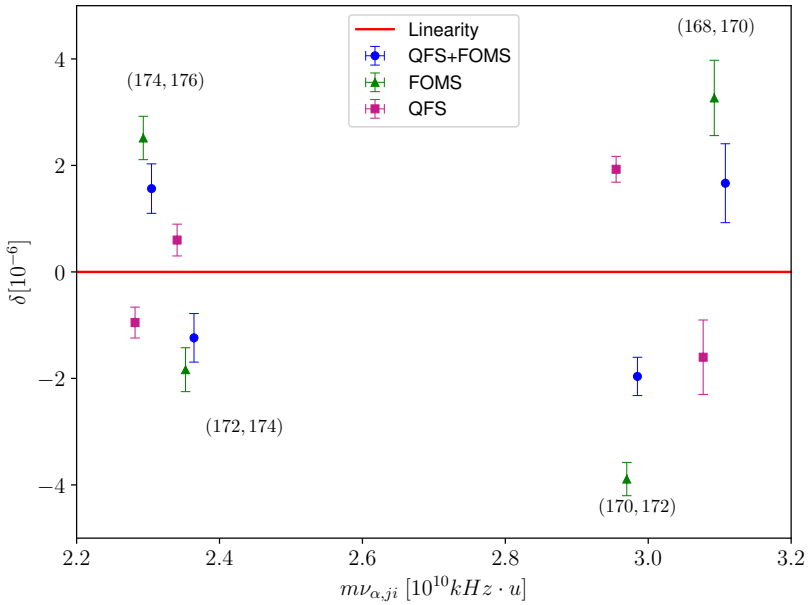

Figure E.5.: Same caption details as fig. E.1 but with UNEDF0 and BCS pairing scheme.

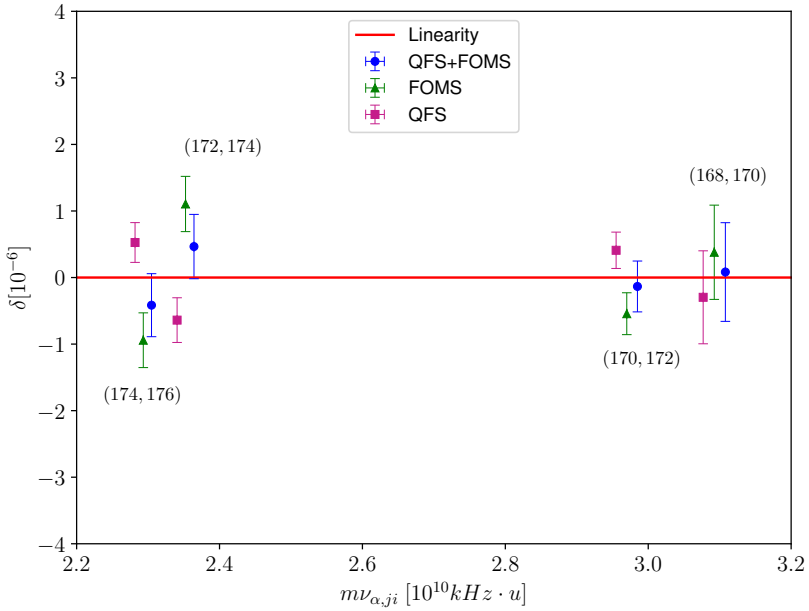

Figure E.6.: Same caption details as fig. E.1 but with UNEDF0 and LN pairing scheme.

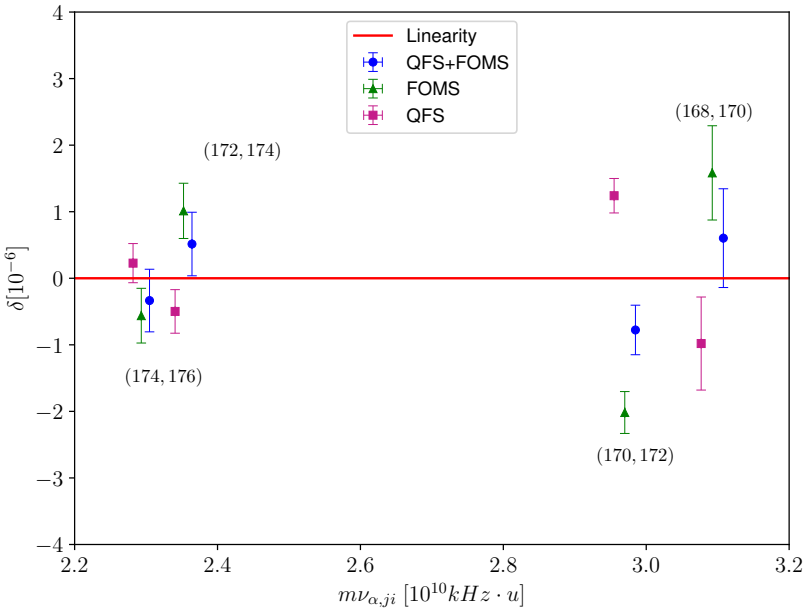

Figure E.7.: Same caption details as fig. E.1 but with UNEDF1 and BCS pairing scheme.

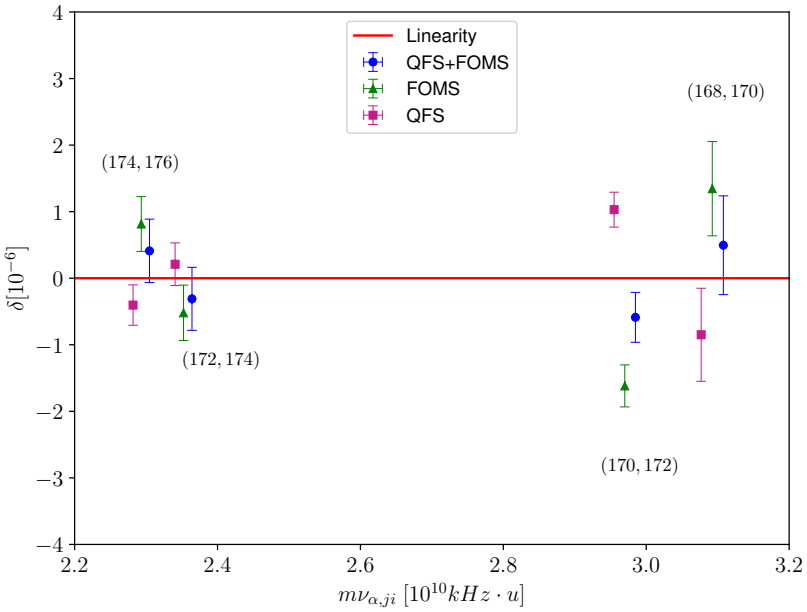

Figure E.8.: Same caption details as fig. 3.7 but using the UNEDF0 parametrisation.

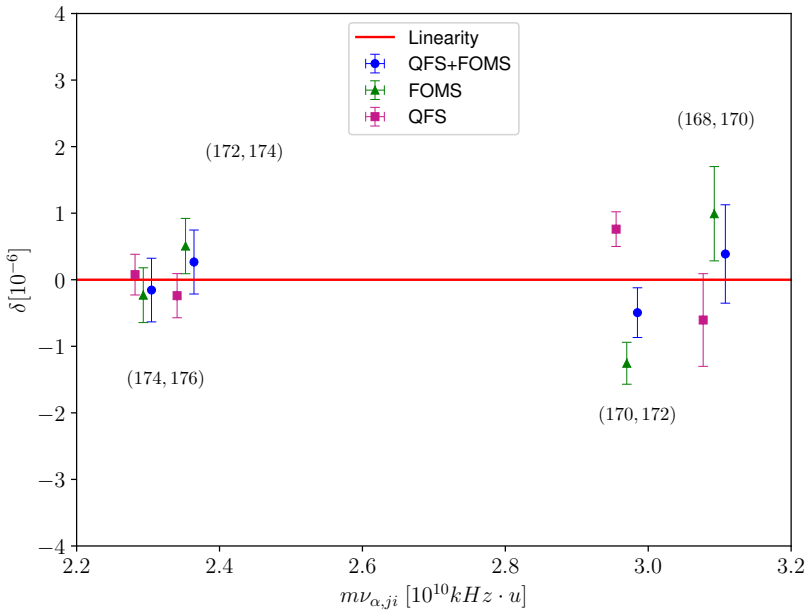

Figure E.9.: Residual deviations from linearity in the King's plot using the SKI3 parametrisation with VDI pairing interaction and a combination of the two pairing schemes (BCS+LN). Theoretical deviations caused by both FOMS and QFS terms are shown as blue circles, while those caused by the QFS term are shown as magenta squares and for the FOMS term as green triangles. The points are shifted from the central $m\nu_{\alpha,ji}$ value for clarity.

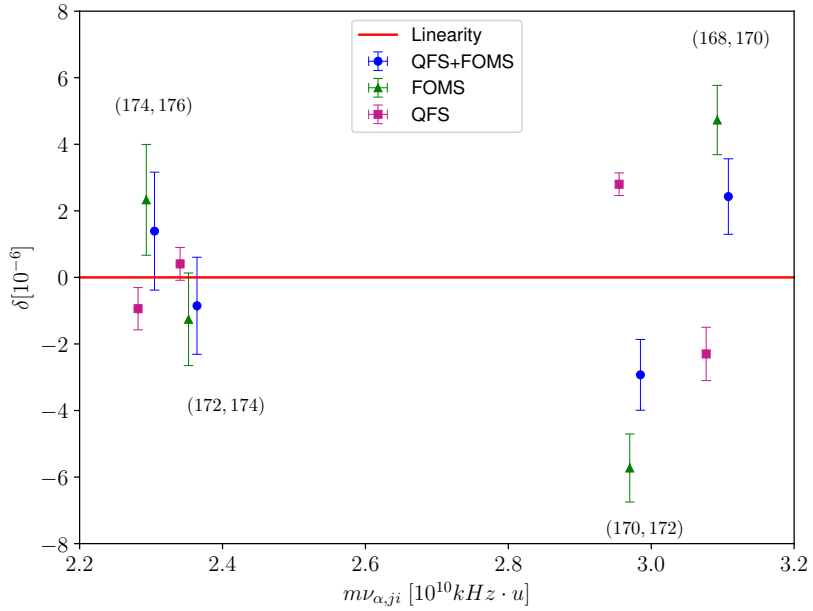

Figure E.10.: Same caption details as fig. E.9 but with the DDDI pairing interaction.

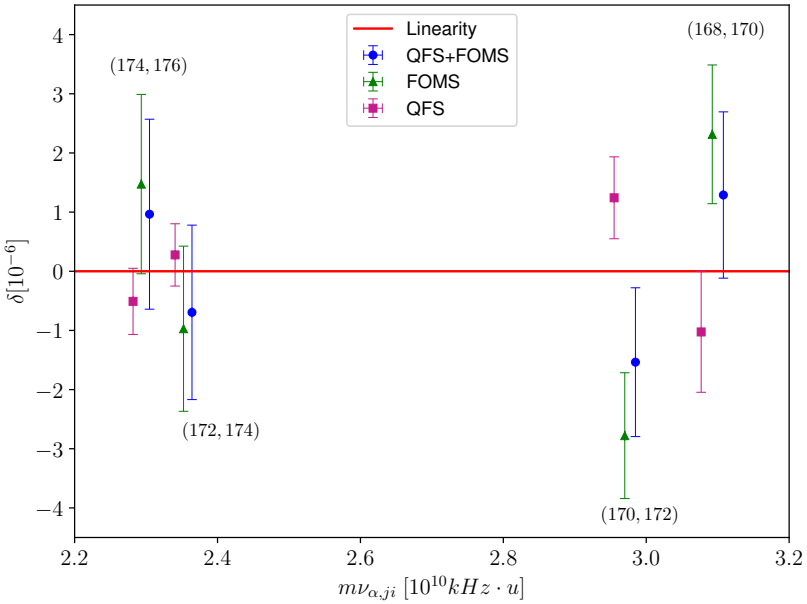

Figure E.11.: Same caption details as fig. E.9 but with the UNEDF0 Skyrme parametrisation.

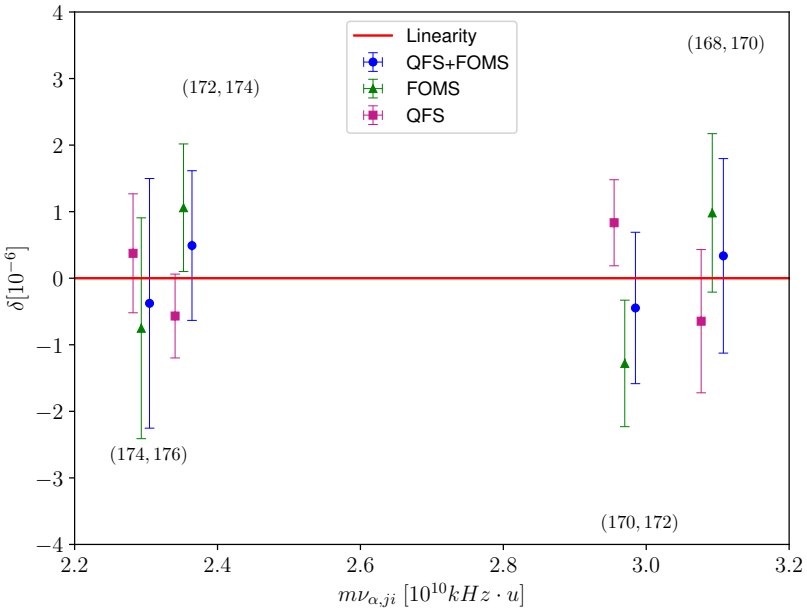

Figure E.12.: Same caption details as fig. E.9 but using the UNEDF1 Skyrme parametrisation.

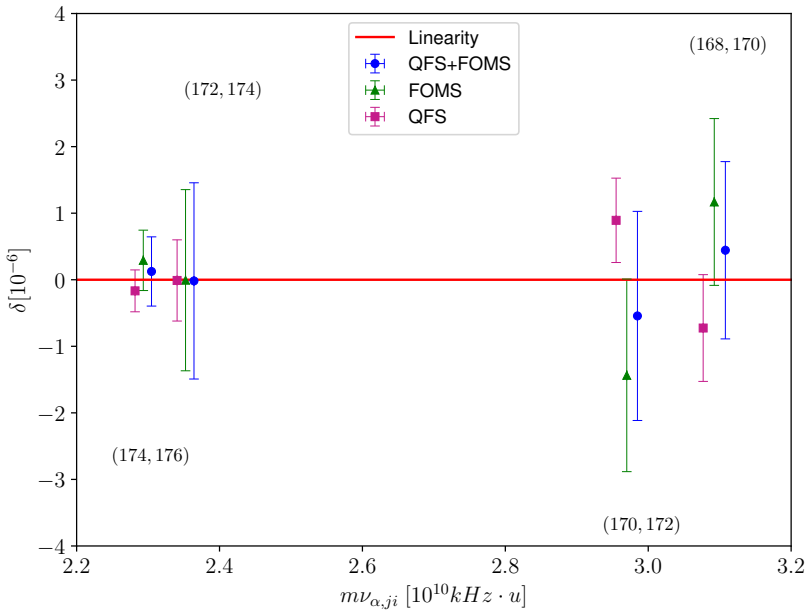

F. Appendix F

In this appendix we present the same tables as section 3.6.1 for the remaining Skyrme parametrisations.

Table F.1.: $\langle r^4 \rangle$-to-$\langle r^2 \rangle$ ratio, b ,see eq. (3.24), for Yb isotopes with the SkI3 Skyrme parametrisation and VDI pairing interaction. $\Delta b/\overline{b}$ stands for the fractional variation, where Δb is the standard deviation of b coefficients divided by their mean value, $\overline{b}$.

Isotope	BCS		LN	
	b	$\Delta b/\overline{b}$	b	$\Delta b/\overline{b}$
^{168}Yb	1.2452		1.2453	
^{170}Yb	1.2468		1.2460	
^{172}Yb	1.2449	0.0019	1.2450	0.0017
^{174}Yb	1.2427		1.2429	
^{176}Yb	1.2409		1.2409	

Table F.2.: Same details as in table F.1 but with SkI3 and DDDI pairing interaction.

Isotope	BCS delta		LN delta	
	b	$\Delta b/\overline{b}$	b	$\Delta b/\overline{b}$
^{168}Yb	1.2452		1.2453	
^{170}Yb	1.2462		1.2461	
^{172}Yb	1.2445	0.0019	1.2447	0.0017
^{174}Yb	1.2422		1.2424	
^{176}Yb	1.2405		1.2407	

Table F.3.: Same details as in table F.1 but with UNEDF0.

Isotope	BCS		LN	
	b	$\Delta b/\overline{b}$	b	$\Delta b/\overline{b}$
^{168}Yb	1.2470		1.2468	
^{170}Yb	1.2471		1.2473	
^{172}Yb	1.2468	0.0010	1.2468	0.0010
^{174}Yb	1.2460		1.2459	
^{176}Yb	1.2448		1.2446	

Table F.4.: Same details as in table F.1 but with UNEDF1.

Isotope	BCS		LN	
	b	$\Delta b/\overline{b}$	b	$\Delta b/\overline{b}$
^{168}Yb	1.2431		1.2425	
^{170}Yb	1.2430		1.2423	
^{172}Yb	1.2420	0.0015	1.2415	0.0013
^{174}Yb	1.2403		1.2402	
^{176}Yb	1.2386		1.2387	

Bibliography

[1] V. C. Rubin, W. K. Ford Jr, and N. Thonnard. Rotational properties of 21 sc galaxies with a large range of luminosities and radii, from ngc 4605/r= 4kpc/to ugc 2885/r= 122 kpc. *The Astrophysical Journal*, 238:471–487, 1980.

[2] D. Clowe, M. Bradač, A. H. Gonzalez, M. Markevitch, S. W. Randall, C. Jones, and D. Zaritsky. A Direct Empirical Proof of the Existence of Dark Matter. *Astrophys. J.*, 648(2):L109–L113, sep 2006.

[3] R. Massey, T. Kitching, and J. Richard. The dark matter of gravitational lensing. *Reports Prog. Phys.*, 73(8):086901, aug 2010.

[4] N. Aghanim, Y. Akrami, F. Arroja, M. Ashdown, J. Aumont, et al. Planck 2018 results. *Astron. Astrophys.*, 641:A1, sep 2020.

[5] I. Counts, J. Hur, D. P. L. Aude Craik, H. Jeon, C. Leung, J. C. Berengut, A. Geddes, A. Kawasaki, W. Jhe, and V. Vuletić. Evidence for Nonlinear Isotope Shift in Yb+ Search for New Boson. *Phys. Rev. Lett.*, 125(12):123002, sep 2020.

[6] C. Delaunay, R. Ozeri, G. Perez, and Y. Soreq. Probing atomic Higgs-like forces at the precision frontier. *Phys. Rev. D*, 96(9):093001, nov 2017.

[7] J. C. Berengut, D. Budker, C. Delaunay, V. V. Flambaum, C. Frugiuele, E. Fuchs, C. Grojean, R. Harnik, R. Ozeri, G. Perez, and Y. Soreq. Probing New Long-Range Interactions by Isotope Shift Spectroscopy. *Phys. Rev. Lett.*, 120(9):091801, feb 2018.

[8] S. O. Allehabi, V. A. Dzuba, V. V. Flambaum, and A. V. Afanasjev. Nuclear deformation as a source of the nonlinearity of the King plot in the Yb+ ion. *Phys. Rev. A*, 103(3):L030801, mar 2021.

[9] P.-G. Reinhard, B. Schuetrumpf, and J.A. Maruhn. The Axial Hartree–Fock + BCS Code SkyAx. *Comput. Phys. Commun.*, 258:107603, jan 2021.

[10] W. H. King. *Isotope Shifts in Atomic Spectra*. Springer US, Boston, MA, 1984.

[11] C. Solaro, S. Meyer, K. Fisher, J. C. Berengut, E. Fuchs, and M. Drewsen. Improved Isotope-Shift-Based Bounds on Bosons beyond the Standard Model through Measurements in Ca+. *Phys. Rev. Lett.*, 125(12):123003, sep 2020.

[12] E. C. Seltzer. X-Ray Isotope Shifts. *Phys. Rev.*, 188(4):1916–1919, dec 1969.

[13] S. A. Blundell, P. E. G. Baird, C. W. P. Palmer, D. N. Stacey, and G. K. Woodgate. A reformulation of the theory of field isotope shift in atoms. *J. Phys. B At. Mol. Phys.*, 20(15):3663–3681, aug 1987.

[14] J. A. R. Griffith, G. R. Isaak, R. New, M. P. Ralls, and C. P. van Zyl. Anomalies in the optical isotope shifts of samarium. *J. Phys. B At. Mol. Phys.*, 12(1):L1–L7, jan 1979.

[15] CJ Horowitz and J Piekarewicz. Impact of spin-orbit currents on the electroweak skin of neutron-rich nuclei. *Physical Review C*, 86(4):045503, 2012.

[16] J. A. Maruhn, P.-G. Reinhard, and E. Suraud. Density Functional Theory. In *Simple Model. Many-Fermion Syst.*, pages 143–161. Springer Berlin Heidelberg, Berlin, Heidelberg, 2010.

[17] M. R. Bhat. Evaluated Nuclear Structure Data File (ENSDF). In *Nucl. Data Sci. Technol.*, pages 817–821. Research Reports in Physics. Springer, Berlin, Heidelberg., 1992.

[18] S. G. Nilsson and I. Ragnarsson. *Shapes and Shells in Nuclear Physics*. Cambridge University Press, 1995.

[19] Zhen-Hua Zhang, Miao Huang, and A. V. Afanasjev. Rotational excitations in rare-earth nuclei: A comparative study within three cranking models with different mean fields and treatments of pairing correlations. *Phys. Rev. C*, 101(5):054303, may 2020.

[20] P. Ring and P. Schuck. *The nuclear many-body problem*. Springer Science & Business Media, 2004.

[21] J. Erler, P. Klüpfel, and P.-G. Reinhard. Self-consistent nuclear mean-field models: example Skyrme–Hartree–Fock. *J. Phys. G Nucl. Part. Phys.*, 38(3):033101, mar 2011.

[22] J. Bardeen, L. N. Cooper, and J. R. Schrieffer. Microscopic Theory of Superconductivity. *Phys. Rev.*, 106(1):162–164, apr 1957.

[23] M. Bender, P.-H. Heenen, and P.-G. Reinhard. Self-consistent mean-field models for nuclear structure. *Rev. Mod. Phys.*, 75(1):121–180, jan 2003.

[24] D. Vautherin and D. M. Brink. Hartree-Fock Calculations with Skyrme's Interaction. I. Spherical Nuclei. *Phys. Rev. C*, 5(3):626–647, mar 1972.

[25] J. Erler, P. Klüpfel, and P.-G. Reinhard. Misfits in Skyrme–Hartree–Fock. *J. Phys. G Nucl. Part. Phys.*, 37(6):064001, jun 2010.

[26] W. Kohn and L. J. Sham. Self-Consistent Equations Including Exchange and Correlation Effects. *Phys. Rev.*, 140(4A):A1133–A1138, nov 1965.

[27] Reiner M. Dreizler and Eberhard K. U. Gross. *Density Functional Theory*. Springer Berlin Heidelberg, Berlin, Heidelberg, 1990.

[28] P. Klüpfel, P.-G. Reinhard, T. J. Bürvenich, and J. A. Maruhn. Variations on a theme by Skyrme: A systematic study of adjustments of model parameters. *Phys. Rev. C*, 79(3):034310, mar 2009.

[29] E. Chabanat, P. Bonche, P. Haensel, J. Meyer, and R. Schaeffer. New Skyrme effective forces for supernovae and neutron rich nuclei. *Phys. Scr.*, T56(T56):231–233, jan 1995.

[30] P.-G. Reinhard and H. Flocard. Nuclear effective forces and isotope shifts. *Nucl. Phys. A*, 584(3):467–488, feb 1995.

[31] M. Kortelainen, J. McDonnell, W. Nazarewicz, E. Olsen, P.-G. Reinhard, J. Sarich, N. Schunck, S. M. Wild, D. Davesne, J. Erler, and A. Pastore. Nuclear energy density optimization: Shell structure. *Phys. Rev. C*, 89(5):054314, may 2014.

[32] M. Kortelainen, J. McDonnell, W. Nazarewicz, P.-G. Reinhard, J. Sarich, N. Schunck, M. V. Stoitsov, and S. M. Wild. Nuclear energy density optimization: Large deformations. *Phys. Rev. C*, 85(2):024304, feb 2012.

[33] P. Fleischer, P. Klüpfel, P.-G. Reinhard, and J. A. Maruhn. Skyrme energy functional and low lying 2+ states in Sn, Cd, and Te isotopes. *Phys. Rev. C*, 70(5):054321, nov 2004.

[34] M. Hoferichter, J. Menéndez, and A. Schwenk. Coherent elastic neutrino-nucleus scattering: EFT analysis and nuclear responses. *Phys. Rev. D*, 102(7):074018, oct 2020.

[35] P.-G. Reinhard and W. Nazarewicz. Nuclear charge densities in spherical and deformed nuclei: Toward precise calculations of charge radii. *Phys. Rev. C*, 103(5):054310, may 2021.

[36] H.H. Ku. Notes on the use of propagation of error formulas. *J. Res. Natl. Bur. Stand. Sect. C Eng. Instrum.*, 70C(4):263, oct 1966.

[37] Raymond T. Birge. The Propagation of Errors. *Am. J. Phys.*, 7(6):351–357, dec 1939.

[38] A. A. Filin, V. Baru, E. Epelbaum, H. Krebs, D. Möller, and P. Reinert. Extraction of the Neutron Charge Radius from a Precision Calculation of the Deuteron Structure Radius. *Phys. Rev. Lett.*, 124(8):082501, feb 2020.

[39] T. Naito, G. Colò, H. Liang, and X. Roca-Maza. Second and fourth moments of the charge density and neutron-skin thickness of atomic nuclei. *Phys. Rev. C*, 104(2):024316, aug 2021.